

A framework for discrete optimization of stellarator coils

K. C. Hammond^{1,*}

¹*Princeton Plasma Physics Laboratory, Princeton, NJ, USA*

Designing magnets for three-dimensional plasma confinement is a key task for advancing the stellarator as a fusion reactor concept. Stellarator magnets must produce an accurate field while leaving adequate room for other components and being reasonably simple to construct and assemble. In this paper, a framework for coil design and optimization is introduced that enables the attainment of sparse magnet solutions with arbitrary restrictions on where coils may be located. The solution space is formulated as a “wireframe” consisting of a mesh of interconnected wire segments enclosing the plasma. Two methods are developed for optimizing the current distribution on a wireframe: Regularized Constrained Least Squares (RCLS), which uses a linear least-squares approach to optimize the currents in each segment, and Greedy Stellarator Coil Optimization (GSCO), a fully discrete procedure in which loops of current are added to the mesh one by one to achieve the desired magnetic field on the plasma boundary. Examples are presented of solutions obtainable with each method, some of which achieve high field accuracy while obeying spatial constraints that permit easy assembly.

I. INTRODUCTION

Stellarators aim to confine hot, dense plasmas using a magnetic field generated entirely by external magnets, without the need to drive current within the plasma. For this concept to work successfully, the magnetic field must be carefully shaped in order to ensure that plasma particles and energy are well confined [1]. Designing magnets to produce a field that meets these shaping requirements typically requires numerical optimization. Optimizing stellarator magnets involves three interconnected components: (1) an objective function that quantifies how well the desired properties have been achieved by a given design, (2) a framework that maps a set of numerical parameters to a magnet design, and (3) an algorithm that adjusts the design parameters in order to find the best possible value of the objective function.

With regard to the second component, magnet optimization problems provide extensive flexibility because there are infinitely many distributions of external sources that can produce a given magnetic field in the vicinity of the plasma [2]. In most stellarator designs these sources are electromagnetic coils, although other sources are possible, including permanent magnets [3] and superconducting monoliths [4]. For an optimization problem to be tractable, the design framework can only sample a portion of this infinite solution space. Correspondingly, many such frameworks are possible, each one encompassing different portions of the space.

One commonly-used framework entails the definition of a toroidal *winding surface* that encloses the plasma and carries a surface current distribution. The surface current can be represented by a scalar current potential function, which is most often parametrized with Fourier coefficients. These parameters can be optimized with a linear least-squares approach in codes such as NESCOIL [5] or REGCOIL [2]. The level curves of the optimized current distribution can form the basis for the design of coils. While the standard application of this framework holds the shape of the winding surface fixed, further improvements can be gained by optimizing the winding surface

itself and/or by directly optimizing the paths taken by the coils along the surface [6–8].

In another framework, the field sources are a set of current-carrying space curves that directly represent the shapes of coils. The space curves may be parametrized, for example, with Fourier coefficients [9, 10] or spline knots [11–13]. The fidelity of the framework to realistic coil design may be improved by modeling coils with finite dimensions [14, 15]. Space curve parameterizations have been optimized with non-linear quasi-Newton codes such as FOCUS [10] or a genetic algorithm as in GOSPEL [12]. Compared to the winding surface approach, the space curve approach has the advantage that the geometry of each coil can be independently parametrized, and optimizers can more easily explore the three-dimensional volume around the plasma. On the other hand, the space curve approach has less topological flexibility, as the number of coils must be predefined.

The exploration of permanent magnet stellarator designs has led to the development of new frameworks for parametrization and optimization. In some cases, the concept of the winding surface is extended to represent a surface of magnetized material of varying thickness. Such surfaces have been optimized using iterated linear least-squares procedures [16–18]. In other frameworks, the solution space consists of an array of independently parametrized magnetic dipoles with arbitrary spatial positions, for which the dipole moments are then optimized using nonlinear continuous procedures [19, 20], and subsequently discretized to minimize the number of unique magnet types [21–23]. Magnetic dipole arrays have also been constructed and optimized using discrete greedy algorithms [24–27].

The representation of permanent magnet solutions as arrays of independent dipoles illustrated the advantages of a spatially local parametrization, which made it easier to design magnet distributions around specific obstacles and optimize for sparsity. More recently, spatially local parametrizations have been explored for distributions of current density as well. Examples include current potential patches defined on 2D winding surfaces [28] and current voxels that fill arbitrary 3D volumes [29].

This paper introduces a new framework for optimizing discrete distributions of current with a spatially local

* khammond@pppl.gov

parametrization. The framework, hereafter referred to as a *wireframe*, consists of an interconnected network of current-carrying wire segments. The parameters for the distribution are simply the currents within each segment; therefore it is straightforward to block off segments lying in arbitrary regions of design space to leave room for other components. While examples in this paper all use wireframes that exhibit two-dimensional topology similar to that of a winding surface, wireframes can in principle be designed to fill arbitrary three-dimensional volumes.

This framework enables multiple optimization strategies, including a rapid linear least-squares approach and a fully discrete greedy approach analogous to greedy algorithms previously used with permanent magnets. As will be demonstrated, the greedy optimizer in particular can be utilized to obtain sparse solutions with arbitrary spatial constraints, yielding starting points for convenient coil designs that could not be easily found using previous methods.

The paper will be organized as follows. Section II will introduce the concept of the wireframe in detail along with the governing equations for calculating the field and setting constraints on its current distribution. Section III will describe the linear Regularized Constrained Least Squares (RCLS) optimization method along with some example solutions that achieve high field accuracy on a relatively coarse wireframe. Section IV will describe the discrete Greedy Stellarator Coil Optimization (GSCO) algorithm and present a number of basic use cases that lead to coil solutions with potentially convenient properties.

II. THE WIREFRAME

The wireframe as defined in this paper is a parametrized solution space for a spatial distribution of electric current. Fundamentally, it consists of a set of interconnected straight segments of filamentary, current-carrying “wire”. Segments connect to one another at *nodes*, and in turn, the location and orientation of each segment is defined by the positions of the two nodes that form its endpoints. Each segment carries a certain current. Thus, the spatial current distribution in a wireframe containing N segments can be fully specified by the positions of its nodes, the pairs of nodes that each segment is connected to, and the current carried by each segment.

An example of a wireframe is depicted in Fig. 1. In this case, the segments of the wireframe join to form a toroidal mesh that encloses a stellarator plasma. The wireframe is constructed by first defining a toroidal reference surface around the plasma. A 2D grid of points spaced regularly in the toroidal and poloidal angles is then placed on the reference surface; these points are defined as the positions of the nodes. The segments are then constructed along straight lines that join adjacent nodes in the toroidal and poloidal grid dimensions. Segments that connect adjacent nodes in the toroidal dimension will be referred to as *toroidal segments*, whereas segments that connect adjacent nodes in the poloidal dimension will be referred to as *poloidal segments*. The wireframes used in this paper will all have toroidal topology, although in

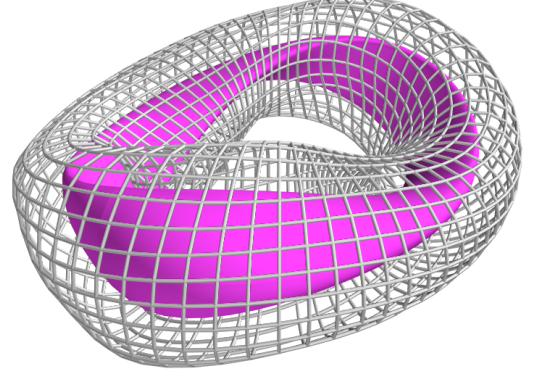


FIG. 1. Example of a wireframe with toroidal topology (gray) enclosing a plasma (magenta).

general wireframes can have other topologies. Furthermore, the wireframes studied here will exhibit stellarator symmetry; thus, for a stellarator with N_{fp} toroidal field periods, a wireframe is fully specified by the segments and currents within one half-period.

The magnetic field at a point \mathbf{p} due to a wireframe segment between nodes located at points \mathbf{p}_1 and \mathbf{p}_2 can be derived from the Biot-Savart law for a filamentary current and is given by [30, 31]

$$\mathbf{B} = \frac{\mu_0 I}{4\pi} \left(\frac{|\mathbf{r}_1| + |\mathbf{r}_2|}{|\mathbf{r}_1||\mathbf{r}_2|(|\mathbf{r}_1||\mathbf{r}_2| + \mathbf{r}_1 \cdot \mathbf{r}_2)} \right) \mathbf{r}_1 \times \mathbf{r}_2, \quad (1)$$

where μ_0 is the vacuum permeability constant, I is the current carried by the segment with positive current defined as flowing from \mathbf{p}_1 to \mathbf{p}_2 , $\mathbf{r}_1 = \mathbf{p} - \mathbf{p}_1$, and $\mathbf{r}_2 = \mathbf{p} - \mathbf{p}_2$. A derivation of this expression is provided in Appendix A.

An important quantity for evaluating the suitability of an externally-generated magnetic field to confine a stellarator plasma is the normal component of the field on the boundary of the desired plasma. Following Eq. 1, the normal component B_{ni} of the magnetic field from the wireframe at a test point \mathbf{p}_i on the plasma boundary can be expressed as a linear combination of the currents in the wireframe’s N segments,

$$B_{ni} = \sum_{j=1}^N G_{ij} x_j, \quad (2)$$

where x_j is the current in the j^{th} segment of the wireframe and G_{ij} contains the geometric terms relating the current to the normal field component:

$$G_{ij} = \frac{\mu_0}{4\pi} \left(\frac{|\mathbf{r}_{1ij}| + |\mathbf{r}_{2ij}|}{|\mathbf{r}_{1ij}||\mathbf{r}_{2ij}|(|\mathbf{r}_{1ij}||\mathbf{r}_{2ij}| + \mathbf{r}_{1ij} \cdot \mathbf{r}_{2ij})} \right) (\mathbf{r}_{1ij} \times \mathbf{r}_{2ij}) \cdot \hat{\mathbf{n}}_i \quad (3)$$

Here, $\hat{\mathbf{n}}_i$ is the unit normal vector at the i^{th} test point on the plasma boundary; while $\mathbf{r}_{1ij} = \mathbf{p}_i - \mathbf{p}_{1j}$ and $\mathbf{r}_{2ij} = \mathbf{p}_i - \mathbf{p}_{2j}$, where \mathbf{p}_{1j} and \mathbf{p}_{2j} are the endpoints of the j^{th} segment.

The methods introduced in this paper seek to optimize the current distribution in the wireframe while keeping its geometry fixed. Therefore, the optimization problem consists of finding an optimal set of currents \mathbf{x} for each segment in the wireframe.

While \mathbf{x} contains N elements – one current for each segment – in general the problem has fewer than N degrees of freedom due to constraints on the current distribution. For example, it is important to impose constraints in order to avoid charge accumulation at the nodes. In other words, the current flowing into each node should equal the current flowing out. For a given node with the label k , this can be expressed as a linear equality constraint:

$$\sum_{j \in S_{+k}} x_j - \sum_{j \in S_{-k}} x_j = 0, \quad (4)$$

where S_{+k} is the set of segments for which positive current flows inward toward node k and S_{-k} is the set of segments for which positive current flows outward from node k . These constraints will be referred to as *continuity constraints* because they impose current continuity and prevent charge accumulation within the wireframe.

Additional constraints may be imposed to ensure that current distributions exhibit certain desired properties. For example, a *poloidal current constraint* imposes a value for the net poloidal current I_{pol} flowing within the wireframe. This ensures that average toroidal magnetic field B_t at a given major radius R within the wireframe has the value $\mu_0 I_{pol} / (2\pi R)$. Assuming that the continuity constraints of Eq. 4 are in effect, this constraint can be formulated by requiring that the sum of the currents flowing through all of the poloidal segments within a row extending toroidally around the wireframe grid equal I_{pol} , as shown by the red segments in Fig. 2. This constitutes one additional linear equality constraint,

$$\sum_{j \in S_{pol}} x_j = I_{pol}, \quad (5)$$

where S_{pol} contains the indices of the poloidal segments. While it is sufficient in principle to apply the constraint to the sum the segment currents in a single toroidal row, two rows must be included in this case to uphold the stellarator symmetry of the current distribution.

Similarly, a *toroidal current constraint* may be imposed to require that the wireframe carry a certain net current I_{tor} in the toroidal dimension. Setting I_{tor} to zero prevents current from flowing helically around the torus, ensuring that the wireframe has no net dipole moment. On the other hand, if I_{tor} and I_{pol} are both set to specific values, this will enforce a certain helicity in the current distribution. Assuming the continuity constraints (Eq. 4) apply, I_{tor} can be constrained by ensuring that the sum of the currents through the toroidal segments in one poloidal column equals I_{tor} , as shown by the blue segments in Fig. 2. This constitutes another linear equality constraint,

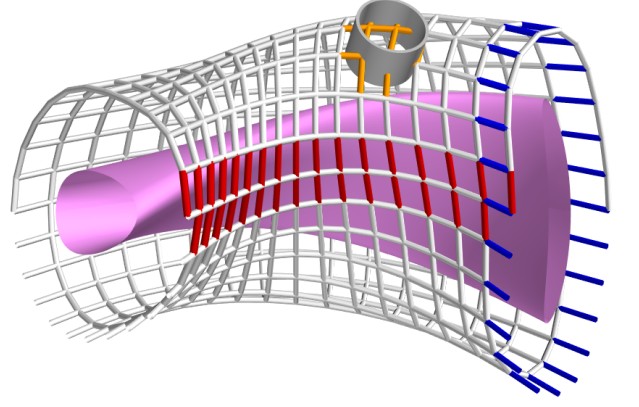


FIG. 2. Schematic of one half-period of a wireframe along with the plasma boundary in magenta and an example diagnostic port in the form of the gray tube. Segments in S_{pol} (Eq. 5) relevant to the poloidal current constraint are shown in red. Segments in S_{tor} (Eq. 6) relevant to the toroidal current constraint are shown in blue. Segments constrained individually to carry zero current (i.e. to avoid collisions with the port) are shown in orange.

$$\sum_{j \in S_{tor}} x_j = I_{tor}, \quad (6)$$

where S_{tor} contains the indices of the toroidal segments in one poloidal column.

Finally, it may be desired to prevent any current from flowing within a given segment. This would be the case, for example, if the segment lies in a spatial region that is reserved for a component such as a port for plasma diagnostics or heating systems. Such a *segment constraint* for a given segment with index j may be expressed simply as

$$x_j = 0 \quad (7)$$

An example set of constrained segments is shown in orange in Fig. 2 to avoid the presence of currents in the vicinity of a port.

Since the constraints described above are all linear equality constraints, any combination of these constraints applicable to a given wireframe may be expressed comprehensively as a system of linear equations,

$$\mathbf{C}\mathbf{x} = \mathbf{d}, \quad (8)$$

where \mathbf{C} is a matrix containing the coefficients of x_j from the left-hand sides of Eq. 4, 5, 6, 7 and \mathbf{d} contains the terms on the right-hand sides of these equations. Formulating the constraints in this way enables the use of constrained linear optimization procedures, such as the one described in Sec. III.

III. REGULARIZED CONSTRAINED LEAST SQUARES (RCLS)

The current distribution in the wireframe can be optimized with many different techniques, each yielding solutions with distinct characteristics and features. This paper will describe two such optimization methods, each of which works to minimize an objective function f through adjustment of the currents \mathbf{x} in the segments of the wireframe. The first method, described in this section, will be called *Regularized Constrained Least Squares* (RCLS). It utilizes a linear least-squares technique that has the advantages of being rapid and non-iterative.

A. Description of the method

For a linear least-squares solver to be applicable, the objective function f must be quadratic in the parameters to be optimized, in this case \mathbf{x} . For the RCLS procedure described in this section the objective function f_{RCLS} is defined as a sum of two sub-objectives:

$$f_{RCLS} = f_B + f_R \quad (9)$$

The first sub-objective, f_B , is a metric of magnetic field error commonly used in stellarator magnet optimization. It is related to the square of the discrepancy from the desired values of the normal component of the magnetic field on the target plasma boundary produced by the wireframe:

$$f_B = \frac{1}{2} (\mathbf{Ax} - \mathbf{b})^2 \quad (10)$$

Hereafter, the square of a vector quantity constitutes the dot product of the vector with itself. \mathbf{A} contains the geometric matrix elements from G as defined in Eq. 3 weighted by the square root of the area a_i of the portion of the target plasma boundary attributed to the respective test point:

$$A_{ij} = G_{ij} \sqrt{a_i} \quad (11)$$

\mathbf{b} contains the desired values of the normal magnetic field at test points on the target plasma boundary, also weighted by $\sqrt{a_i}$:

$$b_i = (\mathbf{B}_{\text{targ},i} \cdot \hat{\mathbf{n}}_i) \sqrt{a_i} \quad (12)$$

The target values of the magnetic field, $\mathbf{B}_{\text{targ},i}$ at each test point on the plasma boundary are the values that the field from the wireframe must attain in order to confine the target plasma, accounting for fixed contributions from other field sources including external coils and currents within the plasma.

As formulated in Eq. 10, f_B is approximately equal to half of the square integral of the field discrepancy over the plasma boundary:

$$f_B \approx \frac{1}{2} \iint [(\mathbf{B}_{\text{wf}} - \mathbf{B}_{\text{targ}}) \cdot \hat{\mathbf{n}}]^2 dA \quad (13)$$

Here, \mathbf{B}_{wf} refers specifically to the magnetic field produced by the wireframe current distribution.

The second sub-objective, f_R , constitutes Tikhonov regularization [32, 33]. It penalizes segment currents that are especially large:

$$f_R = \frac{1}{2} (\mathbf{Wx})^2 \quad (14)$$

\mathbf{W} is a (typically diagonal) matrix of weighting terms. If \mathbf{W} is indeed diagonal and all diagonal elements are the same, then f_R reduces to the form $(1/2)\lambda \mathbf{x}^2$, where λ is the square of each diagonal element. Assigning different values to the diagonal elements of \mathbf{W} , on the other hand, allows the currents in different segments to be weighted differently for the regularization.

The RCLS algorithm finds the optimal set of segment currents \mathbf{x}^* that minimizes the total objective f_{RCLS} while upholding a set of linear equality constraints:

$$\mathbf{x}^* = \min_{\mathbf{x}} (f_B + f_R) \quad (15)$$

$$\text{s.t. } \mathbf{Cx} = \mathbf{d} \quad (16)$$

\mathbf{C} and \mathbf{d} are the left-hand side coefficients and right-hand side terms of the constraint equations as defined in Eq. 8.

The solution \mathbf{x}^* to this problem may be found by solving two systems of linear equations, one with p equations and the other with $n - p$ equations, where p is the number of constraint equations and n is the number of wireframe segments. The procedure is described in more detail in Appendix B.

Mathematically, this approach has much in common with the REGCOIL code for designing stellarator coils [2]. Both approaches use linear least squares to minimize the square integral of the normal field on a target plasma boundary subject to Tikhonov regularization. The difference lies in how the (coil) current distribution is formulated and parametrized. In the case of REGCOIL, the parameters are Fourier coefficients of the current potential of a two-dimensional surface current distribution that encloses the plasma. With RCLS, by contrast, the parameters are the wireframe segment currents and are therefore spatially localized. In addition, in REGCOIL, current continuity is inherently upheld by the current potential formulation; whereas with RCLS, a set of linear equality constraints is required to uphold current continuity.

B. Basic example

An example of a wireframe with currents optimized by the RCLS procedure is shown in Fig. 3. This wireframe encloses the stellarator equilibrium with near-precise quasisymmetry described in Ref. [34] (hereafter “Precise QA”). The equilibrium has two field periods, a major radius of 1 m, and a magnetic field on axis of 1 T. It is a vacuum equilibrium; hence, the

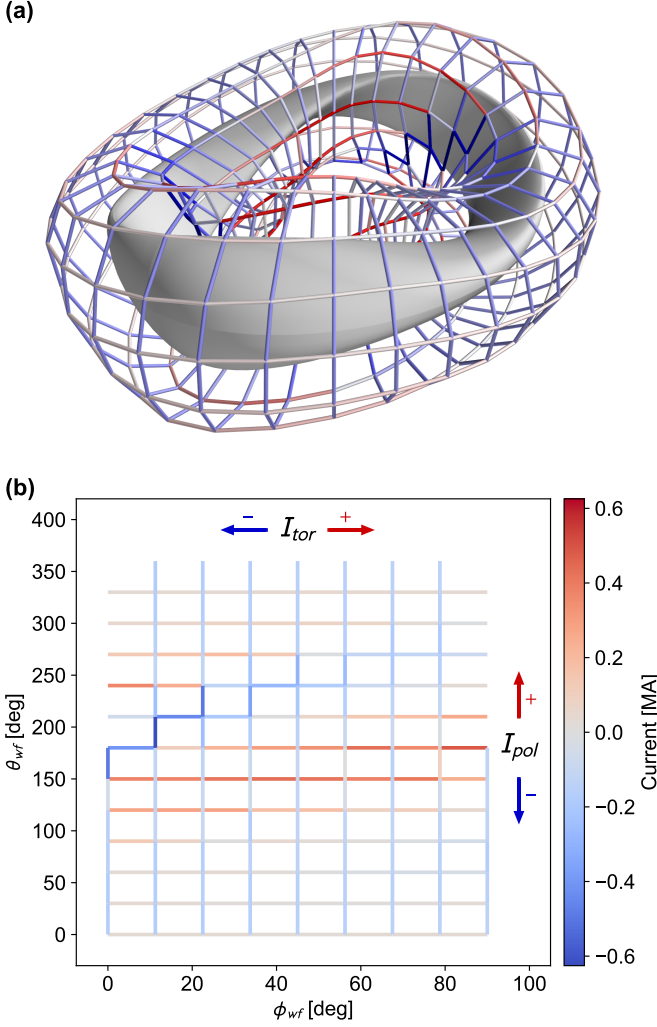


FIG. 3. (a) Rendering of a wireframe with currents optimized to produce a field to confine the Precise QA plasma equilibrium described in Ref. [34], along with the target plasma boundary. Segments are color-coded according to the current they carry. (b) Schematic of the segments of one half-period of the wireframe. Arrows on the top of the plot near “ I_{tor} ” indicate the current flow direction associated with the colors of the horizontal (toroidal) segments; arrows on the right of the plot near “ I_{pol} ” indicate the flow direction associated with the colors of the vertical (poloidal) segments.

pressure is everywhere zero and there are no internal plasma currents. The wireframe was designed such that the nodes are each approximately 0.3 m from the target plasma boundary. Segments and nodes lying in poloidal cross-sections coincide with planes of constant toroidal angle. The segments form a toroidal mesh with $N_{tor} = 8$ nodes per half-period in the toroidal dimension (i.e. 32 nodes per toroidal revolution) and $N_{pol} = 12$ nodes in one poloidal revolution. The resolution of this wireframe will be denoted hereafter as 8×12 or, more generally, $N_{tor} \times N_{pol}$. In general, a half-period contains $N_{tor}N_{pol}$ toroidal segments and the same number of poloidal segments, leading to a total of $2N_{tor}N_{pol}$ segments per half-

period.

For this wireframe, the RCLS procedure optimized the currents in the 192 unique segments constituting a single half-period, which by symmetry specify the currents in all 768 segments within the torus. The segments’ currents were all subject to continuity constraints (Eq. 4), and a poloidal current constraint (Eq. 5) mandated that the net poloidal current flowing in the wireframe equal 5 MA to produce an average toroidal field of 1 T at major radius $r = 1$ m. Altogether, there were 95 constraint equations, leaving 97 degrees of freedom for the optimization. The solution was obtained using a regularization matrix of $\mathbf{W} = (10^{-10} \text{ Tm/A})\mathbf{I}$, where \mathbf{I} is the $n \times n$ identity matrix with $n = 192$ equal to the number of segments. The solution took approximately 100 ms to compute on a laptop computer. All of the equality constraints were very well satisfied, with the largest component of the residual vector $\mathbf{C}\mathbf{x} - \mathbf{d}$ having an absolute value of less than 1×10^{-9} A (for reference, the smallest current carried in any of the wireframe segments had an absolute value of 1.7×10^3 A).

Fig. 3a shows a three-dimensional rendering of the wireframe and the target plasma boundary. Fig. 3b contains a two-dimensional schematic of the segments and currents. The latter figure depicts the segments from one half-period of the wireframe (one-fourth of the torus in this case) flattened out with the toroidal dimension on the horizontal axis and the poloidal dimension on the vertical axis. The coordinates correspond to the toroidal ϕ_{wf} and poloidal θ_{wf} angles at which the nodes appear on the toroidal reference surface used to construct the wireframe (the subscript “wf” is meant to distinguish the wireframe reference surface angles from the angles parametrizing the target plasma boundary). Toroidal segments, which carry current in (approximately) the toroidal dimension, are oriented horizontally; whereas poloidal segments, which carry current in (approximately) the poloidal dimension, are oriented vertically. The plot is periodic in the poloidal (vertical) dimension; hence, the tops of the poloidal segments appearing at $\theta_{wf} = 360^\circ$ are connected to the segments appearing at $\theta_{wf} = 0^\circ$ on the outboard side. The poloidal segments on the left-hand and right-hand sides of the plot (toroidal angles $\phi_{wf} = 0^\circ$ and 90°) lie in symmetry planes at the interfaces between adjacent half-periods; as such, half of the segments in those planes are not shown because they essentially “belong” to the adjacent half-periods in accordance with stellarator symmetry [35].

As indicated by the arrows in the margins of Fig. 3b, the segments are color-coded according to the magnitude and direction of the current they carry. For the toroidal segments, red indicates current flow in the positive toroidal direction (right), whereas blue indicates current flow in the negative toroidal direction (left). Similarly, for the poloidal segments, red indicates current flow in the positive poloidal direction (up), whereas blue indicates current flow in the negative poloidal direction (down).

As can be seen in Fig. 3, every segment carries a unique current. This is a consequence of the linear least-squares optimization approach, in which the free parameters – i.e. the segment currents – are optimized in a continuous space. Nevertheless, current continuity is enforced at each node through

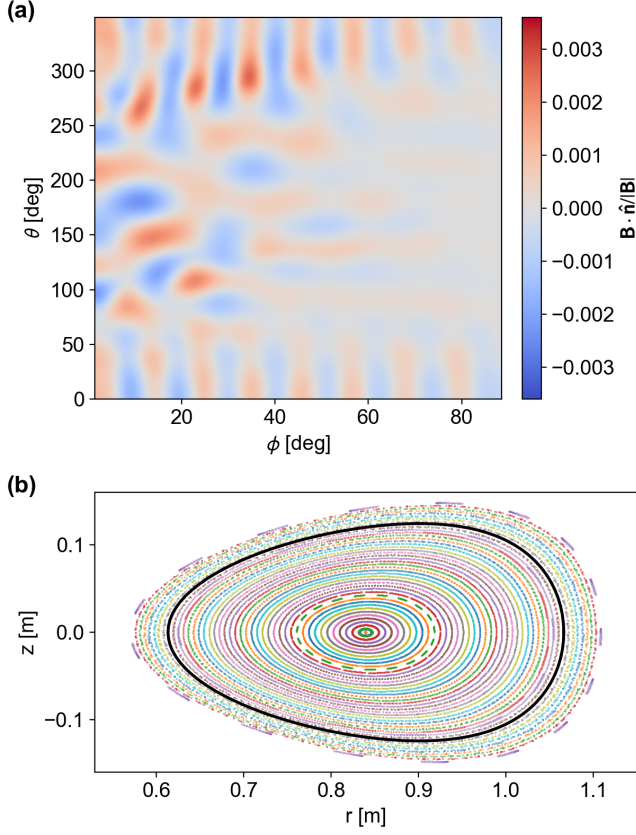


FIG. 4. (a) Normal component of the magnetic field on the plasma boundary produced by the wireframe shown in Fig. 3, relative to the magnitude of the magnetic field. (b) Poincaré cross-section of the magnetic field lines produced by the wireframe solution (dots) along with a cross-section of the target plasma boundary (black curve).

the incorporation of the linear equality constraints in Eq. 4; hence, there is no charge accumulation at the nodes. Also, while no upper bounds are explicitly enforced on the values of the segment currents, the incorporation of Tikhonov regularization effectively restricts how large these currents can be.

Magnetic field accuracy can be quantified by $(\mathbf{B} \cdot \hat{\mathbf{n}})/|\mathbf{B}|$, the relative normal component of the total magnetic field \mathbf{B} (including contributions from the wireframe as well as plasma currents or external magnets if present) on the target plasma boundary. A perfectly accurate field is tangential to the target plasma boundary, and hence $(\mathbf{B} \cdot \hat{\mathbf{n}})/|\mathbf{B}|$ is ideally 0. The magnetic field produced by this wireframe solution is highly accurate, as shown in Fig. 4. Fig. 4a indicates that $(\mathbf{B} \cdot \hat{\mathbf{n}})/|\mathbf{B}|$ rarely exceeds 0.3%. The surface average of the absolute value of this normalized quantity over the target plasma boundary, $\langle |\mathbf{B} \cdot \hat{\mathbf{n}}|/|\mathbf{B}| \rangle$, is 6.31×10^{-4} . Furthermore, the flux surfaces produced by the solution, whose geometry is indicated by the Poincaré cross-sections in Fig. 4b, exhibit excellent agreement with the shape of the target plasma boundary.

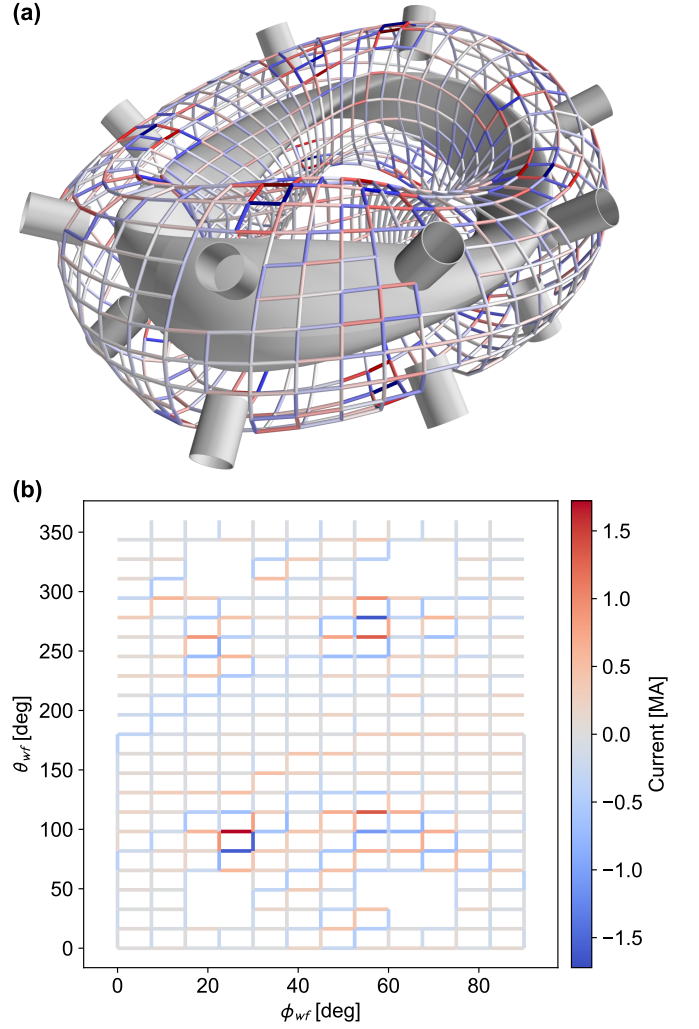


FIG. 5. (a) Rendering of a wireframe with a current distribution optimized with the RCLS technique. Segments constrained to have zero current due to overlap with the cylindrical ports are not shown in the rendering. (b) Schematic of the segments of one half-period, analogous to that of Fig. 3b, not including segments constrained to carry no current.

C. Restricting space for other components

The wireframe formulation makes it straightforward to restrict the solution to have zero current in arbitrary regions, e.g. to leave space for ports and other components. As indicated in Fig. 2, segments that overlap restricted areas can simply be constrained to have zero current by applying segment constraint equations (Eq. 7).

A wireframe solution for the Precise QA plasma with certain areas blocked off for ports is shown in Fig. 5. In this example, each half-period has four cylindrical ports placed on the outboard side. To match the accuracy of the solution without ports as shown in Fig. 3, it was necessary to increase the wireframe grid resolution to 12×22 , presumably to compensate for the spatial gaps in the current distribution introduced

by the segment constraints. Accounting for the constraints placed on continuity, poloidal current, and the segments that collide with ports, the wireframe has 241 degrees of freedom to be optimized. For this solution, the regularization matrix was $\mathbf{W} = (10^{-10} \text{ Tm/A})\mathbf{I}$, where \mathbf{I} is the $n \times n$ identity matrix with $n = 528$ equal to the number of segments.

Fig. 5 shows the current distribution in the wireframe determined for this solution. Segments carrying zero current as a result of being constrained are omitted. While the overall field accuracy metric $\langle |\mathbf{B} \cdot \hat{\mathbf{n}}| / |\mathbf{B}| \rangle$ is 6.37×10^{-4} , nearly the same as that of the no-port solution, the solutions exhibit some differences. First, the maximum segment current in this solution is roughly twice that of the no-port solution, with the largest currents appearing in the vicinity of the holes in the distribution at the locations of the ports. Another contrast with the no-port solution is in the net toroidal current, which was not constrained for either solution. For this solution, the net toroidal current was 0.65 MA, whereas it was 0.90 MA in the no-port case.

It is notable that wireframes with RCLS solutions are able to achieve high magnetic field accuracy with a relatively coarse grid with few degrees of freedom, particularly in the no-port case. However, it is not clear how practical these solutions would be to implement. While each individual straight segment of the wireframe is conceptually simple, driving unique currents through the many segments, each of which has junctions with other segments carrying different currents, would be challenging. Nevertheless, RCLS can be useful as a means of rapidly constructing a highly accurate vacuum magnetic field for a given plasma equilibrium. In addition, RCLS may be used to optimize the currents in pre-defined paths within the wireframe, separated from one another with segment constraints that prevent the existence of multi-current junctions.

IV. GREEDY STELLARATOR COIL OPTIMIZATION (GSCO)

The RCLS method is just one of many optimization approaches that can be employed within the wireframe solution space. This section introduces a new, fully discrete optimization technique, hereafter referred to as *Greedy Stellarator Coil Optimization* (GSCO). GSCO is an iterative method that constructs paths of current within the wireframe that can form the basis for the design of coils.

A. Description of the method

The GSCO procedure works by adding small loops of current to the wireframe, one by one. For the present work, these current loops encircle single *cells* of the wireframe grid. Each cell consists of four segments that surround a quadrilateral gap; in other words, the segments forming a cell do not enclose any other segments.

Fig. 6 illustrates schematically how coils may be constructed on a wireframe by adding loops of current. In Fig. 6a,

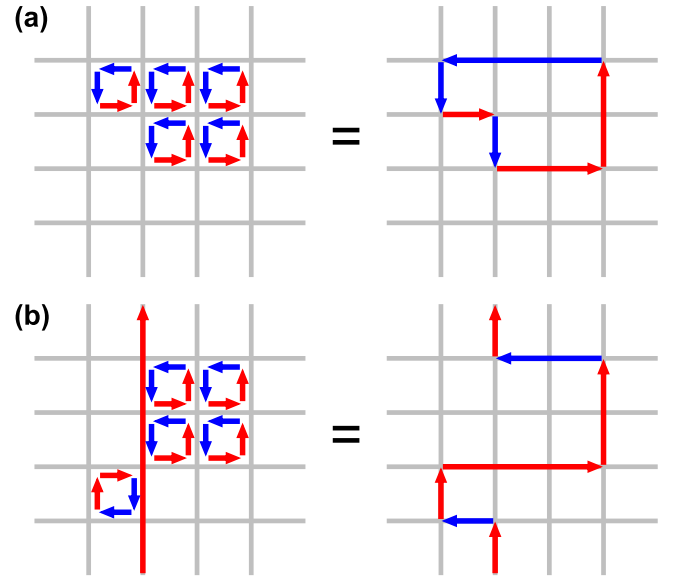


FIG. 6. Schematic illustrations of how adding loops of current can effectively add or reshape coils in a wireframe grid. (a) Adding loops of current with the same polarity to a set of contiguous cells creates a saddle coil. (b) Adding loops of current next to a pre-existing straight section of a coil can add curvature to the coil.

five loops with the same polarity are added to five contiguous cells of the wireframe. Note that the net current in segments between adjacent loops is zero, as the contributions from the two loops are equal and opposite. Accounting for these cancellations, the net effect of the five loops is to create a saddle coil enclosing the cells where the loops were added.

Fig. 6b shows how a pre-existing section of a coil can be reshaped by adding current loops to cells adjacent to the coil. In this case, the pre-existing coil is represented by the straight, vertical current flow. If loops of current are added adjacent to this coil, and the magnitude and polarity of these loops is such that the loops cancel out the current in the initially active coil segments, the net effect is to divert the initial flow along a new path, as seen in the right-hand plot.

The process of adding loops of current to the wireframe thus constitutes a topologically flexible method of designing coils. New coils can be created by adding loops of current to an empty section of the wireframe, as in Fig. 6a. Existing coils can be reshaped by adding loops of current to adjacent cells, as in Fig. 6b. Furthermore, existing coils can be removed altogether. For example, the coil created by the five counter-clockwise current loops in Fig. 6a can be removed by adding five clockwise current loops to the same cells, effectively cancelling out the contributions of the original counter-clockwise loops.

The GSCO algorithm optimizes the current distribution in a wireframe by performing a series of iterations. In each iteration, a single loop of current is added to the wireframe, with the cell (location) and polarity chosen to bring about the greatest possible reduction in an objective function f_{GSCO} . The

classification of the algorithm as “greedy” arises from its general approach of constructing a solution to a highly complex problem in multiple small steps, in each step making an optimal choice according to a relatively simple heuristic [36].¹ Similar approaches have been used successfully in many applications including signal processing [37], DNA sequencing [38], and operations research [39].

The GSCO procedure draws particular inspiration from the greedy algorithms developed in Refs. [24–27] for designing arrays of permanent magnets to shape the confining fields for stellarator plasmas. The greedy permanent magnet optimizers (GPMO) worked by adding permanent magnets one by one to achieve the desired field shaping. A small loop of current in a wireframe functions similarly to a permanent magnet, in the sense that both constitute sources of approximately dipolar magnetic fields. A wireframe current loop can also be thought of as a discrete analogue to the recently introduced concept of a current potential patch [28]. Arrays of small dipole sources can in principle create highly accurate 3D shaping for stellarator magnetic fields, provided the dipoles are placed in the correct locations with the correct orientations and strengths [3, 19]; this insight forms the basis of the heuristic that guides the iterations in both GPMO and GSCO.

During the greedy iterations, the optimizer faces some limitations on where it may place loops of current. These limitations are defined by a set of eligibility rules that dictate whether any given cell in the wireframe may receive a loop of current. Some possible eligibility rules are summarized in Table I. One essential eligibility rule is that the wireframe current distribution must adhere to the segment constraints (Eq. 7). Clearly, if adding a current loop to a given cell would result in a nonzero current appearing in a constrained segment, that cell should not be eligible. Other eligibility rules are optional and can be used to make the solution simpler. For example, the user can require that solutions exhibit no crossing current paths; i.e. at each node in the wireframe, there can be at most two current-carrying segments. With this requirement in place, any cell for which an added loop of current would result crossed or forked current paths at a node (i.e. in which more than two segments at a node carry current) is not eligible. Note that a cell may be eligible to receive a loop of current with one polarity but not the other, depending on the currents initially flowing in the cell’s segments.

An example of a loop creating a forked current path is shown in Fig. 7. In this example, three loops of current are added next to a straight flow of current. The loops of current are polarized such that they add to, rather than cancel, the current in the segments originally carrying the straight flow. Hence, the net result is a current distribution in which two segments carrying one unit of current feed into a section carrying two units of current at the bottom of the figure, which in turn splits off into two segments carrying one unit of cur-

Rule	Description
wireframe constraints	Solution must satisfy all constraint equations $\mathbf{C}\mathbf{x} = \mathbf{d}$
no crossings	At each node, at most two segments may carry current
no new coils	Loops may not be added to a cell around which all segments presently carry no current
max current (I_{\max})	The absolute value of the current in any segment may not exceed a given I_{\max}
max loops per cell (N_{\max})	The net number of positive or negative loops of current added to a given cell may not exceed a defined maximum N_{\max}

TABLE I. Eligibility rules that may be applied to determine whether a loop of current may be added to a given cell during a GSCO iteration.

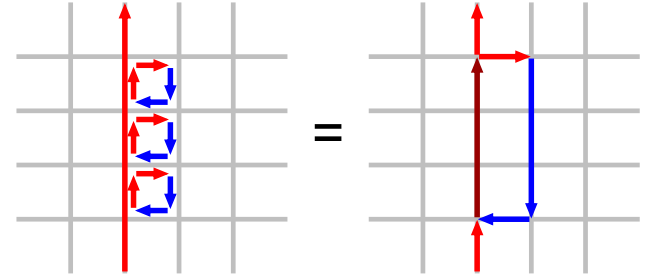


FIG. 7. Illustration showing how the addition of loops of current next to an existing straight section of wire may create a forked current path. In this case, the current loops add to a previously existing current flow rather than canceling it out as in Fig. 6b.

rent at the top. Such distributions can be undesirable if one is seeking a solution with clearly defined, distinct coils whose windings don’t merge together or split apart.

The iterations in GSCO proceed until one of two stopping conditions is reached. The first possible stopping condition is that there are no more cells in the wireframe that are eligible to have a current loop added. The second possible stopping condition is that the optimization has reached a minimal value of the objective function f_{GSCO} . In practice, one can determine that this minimal value has been reached if the optimal current loop determined in a given iteration cancels out the current loop added in the previous iteration. This implies that any subsequent iterations would simply oscillate between two solutions by adding and removing the same current loop. Reaching this stopping condition does not necessarily imply that the absolute minimum of the objective function has been found; rather, the optimizer has become “trapped” in a local minimum of the optimization space.

The objective function f_{GSCO} to be minimized by the GSCO procedure takes weighted contributions from two sub-objectives:

¹ GSCO may also be classified as a repeated *local search*, as the current distribution \mathbf{x} is a feasible solution (i.e. all constraints are obeyed) at every iteration and thus each iteration entails making a small change to an already-feasible solution.

$$f_{\text{GSCO}} = f_B + \lambda_S f_S \quad (17)$$

Here, f_B is the square integral of the normal magnetic field at the plasma boundary as defined in Eq. 10. λ_S is a weighting factor. The second sub-objective f_S is defined as follows:

$$f_S = \frac{1}{2} N_{\text{active}}, \quad (18)$$

where N_{active} is simply the number of segments in the wireframe that are active (i.e. they carry nonzero current). Solutions with lower values of f_S are more sparse than solutions with higher values; thus the objective function incentivizes sparsity in the solution. Sparse solutions are desirable because they are typically simpler to implement and leave more design space available for other components. Optimizations with greater values of λ_S will prioritize sparsity over field accuracy, whereas optimizations with lower values of λ_S will prioritize accuracy over sparsity.

It should be noted that adding a loop of current to the wireframe will not necessarily increase the value of f_S . The impact of a current loop on the sparsity of a solution depends on the current distribution in the wireframe before the loop is added. The possible effects of adding a current loop are illustrated in Fig. 8, which depicts the addition of a current loop in three different locations around an initial current distribution. In Fig. 8a, in which the current loop is added next to a straight section, the result is to cancel the current in the segment that was previously within the straight section and add current to the three segments that were initially inactive. This leads to a net increase of two active segments, or an increase of f_S by 1. In Fig. 8b, a current loop is added next to a corner of the initial current path. In this case, two initially active segments are cancelled and two initially inactive segments are made active, resulting in no net change in f_S . Finally, in Fig. 8c, a current loop is added to the inside of a c-shaped “curve” in the current path. This addition cancels the currents in three initially active segments and imparts current in one initially inactive segment, resulting in a net reduction of two active segments, or a decrease of f_S by 1.

As an aside, note that in each case shown in Fig. 8, the polarity of the added current loop was chosen such that there would be no forked current paths in the final current distributions. Had the polarities of the loops been reversed in any of the three cases, the final current distributions would have exhibited segments with twice the initial current and forks in the current paths. Such cases could be prevented, for example, by the “no crossing” eligibility rule described above and in Table I.

The basic GSCO procedure is summarized formally in Algorithm 1. The required inputs include \mathbf{A} and \mathbf{b} (Eq. 10) for the computation of the objective function as well as \mathbf{C} and \mathbf{d} (Eq. 8) to evaluate the constraints on the segments for determining eligibility. An additional input is a set of vectors $\{\mathbf{u}_i | 1 \leq i \leq \# \text{ cells in wireframe}\}$, each of which encodes a unit current in four segments around a given wireframe cell. Thus, if a wireframe initially has a current distribution represented

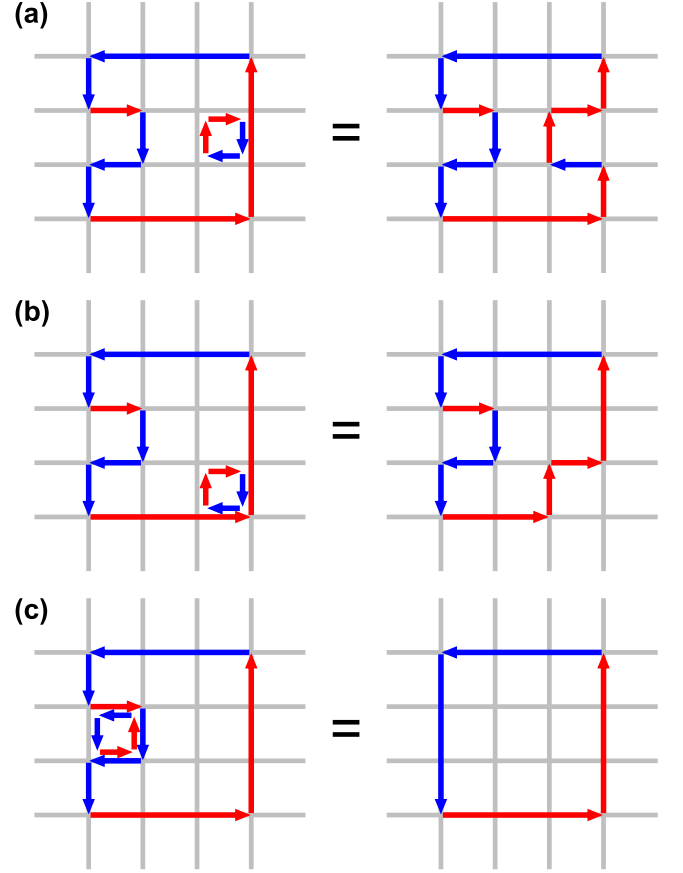


FIG. 8. Depictions of the different ways in which the addition of a current loop can affect the non-sparsity objective f_S of the current distribution in a wireframe: (a) a net increase of two active segments, corresponding to an increase of f_S by 1; (b) no change in the number of active segments or f_S ; (c) a net decrease of two active segments, corresponding to a decrease of f_S by 1.

by \mathbf{x} , the modified current distribution obtained by adding a loop of current I_{loop} to the i^{th} wireframe cell can be expressed as $\mathbf{x} \pm I_{\text{loop}} \mathbf{u}_i$, where the sign specifies the polarity of the loop. With this background data in place, the outcome of GSCO is shaped by the initial current distribution \mathbf{x}_{init} , the loop current I_{loop} , the sparsity weighting parameter λ_S , and the set of eligibility rules chosen from Table I (denoted as RULES) determining where loops may be added.

With the inputs and hyperparameters defined, the algorithm proceeds to add loops of current iteratively to the solution. Each iteration consists of two steps. The first is to build up a set L of possible current loops to add to the solution \mathbf{x} . This entails checking, for each wireframe cell, whether a loop of current $\pm I_{\text{loop}}$ in that cell is eligible to be added according to the rules. If a loop with current I_{loop} is eligible to be added to the i^{th} cell, for example, then the vector $I_{\text{loop}} \mathbf{u}_i$ is added to L . After L is populated, the second step is to choose the optimal member $\mathbf{y}^* \in L$ that achieves the lowest value of the optimization objective f_{GSCO} when added to the present solution. The solu-

Algorithm 1: Greedy Stellarator Coil Optimization (GSCO)

Input: $\mathbf{A}, \mathbf{b}, \mathbf{C}, \mathbf{d}, \{\mathbf{u}_i | 1 \leq i \leq \# \text{ cells in wireframe}\}$
Output: Optimized wireframe currents (\mathbf{x})
function GSCO($\mathbf{x}_{\text{init}}, I_{\text{loop}}, \lambda_S, \text{RULES}$)
 $\mathbf{x} = \mathbf{x}_{\text{init}}$
 repeat
 $L = \{\}$
 for $i = 1, \dots, \# \text{ cells in wireframe}$ **do**
 if $\mathbf{x} + I_{\text{loop}}\mathbf{u}_i$ obeys all RULES **then**
 $L = L \cup \{I_{\text{loop}}\mathbf{u}_i\}$
 end
 if $\mathbf{x} - I_{\text{loop}}\mathbf{u}_i$ obeys all RULES **then**
 $L = L \cup \{-I_{\text{loop}}\mathbf{u}_i\}$
 end
 end
 $\mathbf{y}^* = \min_{\mathbf{y} \in L} [f_B(\mathbf{x} + \mathbf{y}) + \lambda_S f_S(\mathbf{x} + \mathbf{y})]$
 $\mathbf{x} = \mathbf{x} + \mathbf{y}^*$
 until no eligible cells exist or f_{GSCO} stops decreasing
 return \mathbf{x}
end

tion \mathbf{x} is then updated to $\mathbf{x} + \mathbf{y}^*$. The iterations continue until a stopping condition is met; namely, that no eligible cells exist or f_{GSCO} stops decreasing as described above. Note that the set L of eligible current loops must be reconstructed after every iteration, as some rules depend on the current distribution encoded by \mathbf{x} and thus a cell that was eligible in one iteration will not necessarily remain eligible in a subsequent iteration.

Throughout this section, “coils” will be used as shorthand to describe isolated, filamentary paths of current flowing through the wireframe. These paths, which contain many sharp, angular turns, would not necessarily constitute feasible coil geometry – especially if it is desired to make the coils with high-temperature superconducting tape, which cannot tolerate sharp bends [40, 41]. However, they could form a starting point for more realistic coil designs. For example, a wireframe current path with sharp angles could be converted to a smoother curve using splines. Furthermore, these smoothed coil shapes could be refined for improved field accuracy and other objectives with an optimizer such as FOCUS [10], DESC [42], GOSPEL [12], or SIMSOPT [43].

The GSCO procedure can design coils in many different styles and topologies depending on how it is initialized and constrained. In the following sections, some example solutions will be presented to demonstrate some of the possibilities.

B. Modular coils

The GSCO algorithm will first be applied to the design of modular coils for the Precise QA equilibrium. Modular coils, which encircle the plasma once poloidally while remaining toroidally localized, are employed in most modern stellarator designs.

It is important to note that the GSCO algorithm as formu-

lated in Sec. IV A cannot itself create new modular coils on an empty toroidal wireframe grid. Since the incremental current loops added during each iteration cannot, by construction, encircle the plasma, no sum of these loops can contribute a net poloidal current. However, if the wireframe is initialized with some poloidal current flows, GSCO can reshape those flows to create an accurate magnetic field.

Fortunately, the initial poloidal flows need not be complicated. In particular, they may take the form of simple poloidally-flowing rings within the wireframe. The only requirement is that the sum of the currents in these initial flows must equal the net poloidal current corresponding to the desired average toroidal magnetic field on axis.

One example initialization is shown in Fig. 9a. The wireframe used in this case has a grid resolution of 96×100 , which is much greater than the resolutions used for the RCLS solutions in Sec. III. The higher resolution used for the GSCO solutions in this section compensates for the much more stringent limitations that the GSCO solver effectively places on the currents that can be carried by each segment. The wireframe is initialized to have six planar poloidal loops of current per half-period, or twenty-four poloidal loops altogether. The initial loops are spaced evenly in the toroidal angle. The segments in the poloidal current loops each carry 0.208 MA, adding to a total of 5 MA of poloidal current.

A series of optimizations was performed, using GSCO from this initialization of the wireframe, with different values of the weighting parameter λ_S . In each optimization, the eligibility rule preventing crossing current paths was in effect. In addition, the current used in each loop to be added to the wireframe matched the magnitude of the current in the initialized planar poloidal coils. This way, loops could be added next to those initialized coils to modify their shapes without creating forked current paths, similarly to the example in Fig. 6b. Current loops were also eligible to be added to inactive segments in the spaces between existing coils, thereby creating new saddle coils.

The trends in the sub-objective functions over the course of the optimizations for three selected values of λ_S are shown in Fig. 10. In every case, the optimizations terminated upon reaching a minimal value of the total objective function f_{GSCO} . As expected, lower values of λ_S tend to result in solutions with higher field accuracy (lower f_B) and lower sparsity (higher f_S). Interestingly, for the intermediate value of $\lambda_S = 10^{-6} \text{ T}^2\text{m}^2$, both sub-objectives decrease simultaneously during roughly half of the iterations.

The plots in Fig. 9b-d show the results of a series of optimizations using different values of the sparsity weighting factor λ_S . Each optimization began from the same planar loop initialization shown in Fig. 9a. The solutions differ starkly, both in terms of the qualitative appearance of the current distribution (left and center columns) and in terms of the field accuracy (right column).

For the lowest value of λ_S ($10^{-9} \text{ T}^2\text{m}^2$, Fig. 9b), the current distribution has a highly intricate appearance. The inboard side of the wireframe is nearly filled with active segments, forming a dense network of current paths consisting of both modular coils that encircle the plasma and saddle coils that

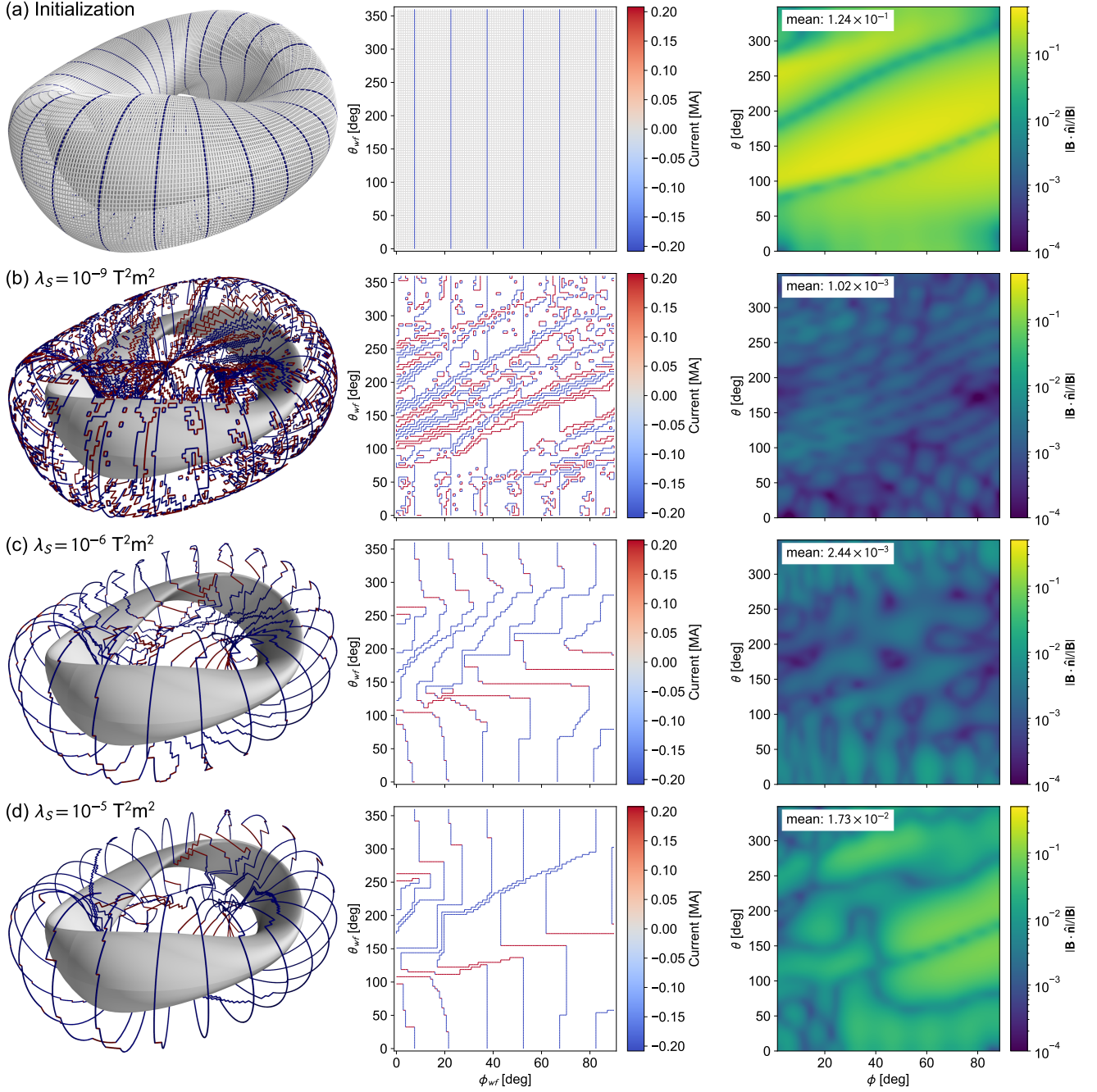


FIG. 9. Current distributions (left and center column) and relative normal magnetic fields on the target plasma boundary (right column) for (a) a wireframe initialized with planar coils, and GSCO solutions using (b) $\lambda_S = 10^{-9} \text{ T}^2\text{m}^2$, (c) $\lambda_S = 10^{-6} \text{ T}^2\text{m}^2$, and (d) $\lambda_S = 10^{-5} \text{ T}^2\text{m}^2$. In subplots (b)-(d), inactive wireframe segments are hidden. The plots in the middle and right columns each represent one half-period of the wireframe and the plasma boundary, respectively.

do not. The outboard side is less dense with current-carrying segments but still features areas packed densely with saddle coils. The solution includes a number of miniature saddle coils that enclose just one or two cells of the wireframe. On the other hand, the solution achieves the best field accuracy metrics, with a surface-averaged relative normal field on the

target plasma boundary of $\langle |\mathbf{B} \cdot \hat{\mathbf{n}}|/|\mathbf{B}| \rangle = 1.02 \times 10^{-3}$.

For the intermediate value of λ_S ($10^{-6} \text{ T}^2\text{m}^2$, Fig. 9c), the current distribution is much more sparse. It consists almost purely of six modular coils per half period, with the exception of one small saddle coil near $\phi_{wf} = 20^\circ$ and $\theta_{wf} = 140^\circ$. Thus, in this case, the predominant effect of GSCO was to reshape

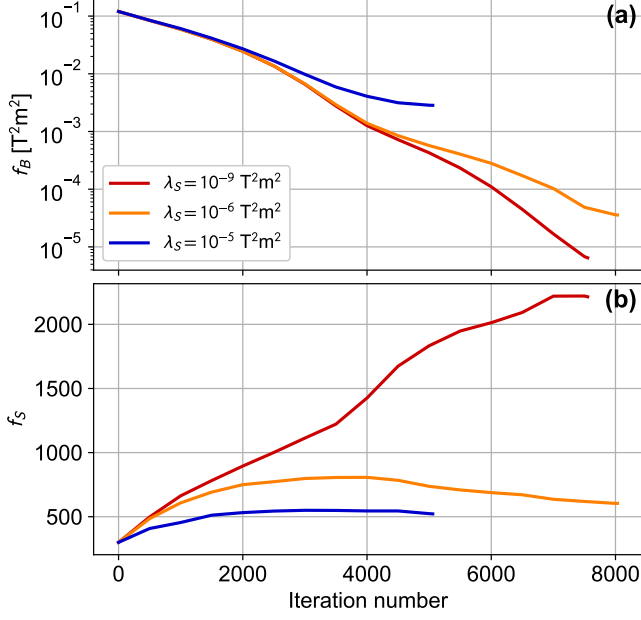


FIG. 10. Values of sub-objective functions over the course of the iterations for GSCO performed on a modular coil initialization with different values of the weighting factor λ_S . (a) f_B ; (b) f_S .

the planar coils from the initialization rather than to add lots of new saddle coils. Overall, the solution has 72% fewer active segments than the solution with $\lambda_S = 10^{-9} \text{ T}^2\text{m}^2$. The increase in sparsity and simplicity came at the expense of some field accuracy, with $\langle |\mathbf{B} \cdot \hat{\mathbf{n}}| / |\mathbf{B}| \rangle$ increasing to 2.44×10^{-3} .

For the highest value of λ_S ($10^{-5} \text{ T}^2\text{m}^2$, Fig. 9d), the current distribution is even more sparse, and this time is a true modular coil solution with no saddle coils present. However, $\langle |\mathbf{B} \cdot \hat{\mathbf{n}}| / |\mathbf{B}| \rangle$ increased substantially relative to the previous case, to 1.73×10^{-2} .

In the solutions using $\lambda_S = 10^{-6}$ and $10^{-5} \text{ T}^2\text{m}^2$, it is notable that many of the initialized planar coils underwent little to no geometric modification on the outboard side (see, in particular, Fig. 9c-d where $\theta_{wf} < 100^\circ$ and $\theta_{wf} > 300^\circ$). This is reminiscent of a pilot plant design described in Refs. [11, 44]. For that design, the COILOPT++ code was employed to optimize the geometry of the modular coils, modeled as spline curves with constraints applied to be mostly vertical on the outboard side. In the GSCO solutions shown here, by contrast, no specific constraints were applied to keep the coils vertical on the outboard side; rather, this geometry is an indirect result of the application of the sparsity objective and the natural tendency for more shaping to be required on the inboard side of most stellarator designs.

The optimizations shown in Fig. 9c-d were performed using 64 cores on a 2.9 GHz Intel Cascade Lake processor node on the Stellar cluster at Princeton University [45]. The wall clock times ranged from 44 seconds ($\lambda_S = 10^{-9} \text{ T}^2\text{m}^2$) to 75 seconds ($\lambda_S = 10^{-6} \text{ T}^2\text{m}^2$), corresponding to 0.8 to 1.3

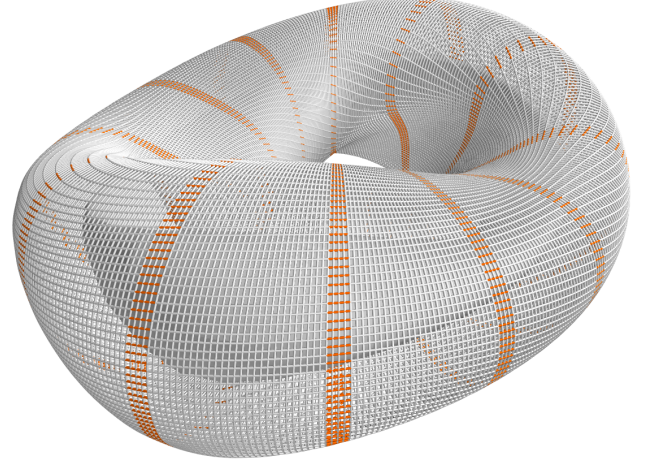


FIG. 11. Depiction of a wireframe with sector constraints that prevent current from crossing certain planes of constant toroidal angle. The constrained segments, through which no current may flow, are shown in orange.

CPU-hours. In each case, the wireframe contained a total of 19,200 segments per half-period, and 1,024 field evaluation points were used in the target plasma boundary to evaluate f_B .

Before proceeding with further optimization results, it is worthwhile to note the extent to which the geometry of the wireframe, which remains fixed during each optimization, can affect the quality of the solutions. In some cases, even subtle changes in the wireframe geometry can have a noticeable impact on the achievable flux surface quality. This is discussed in more detail in Appendix C.

C. Sector-confined saddle coils

While the modular coil optimizations in Sec. IV B serve as a useful proof-of-concept for the GSCO procedure, they do not utilize a key feature of GSCO; namely, the ability to impose arbitrary spatial restrictions on where coils may appear. Such restrictions enable the development of designs that explicitly reserve space for other device components or facilitate easier assembly and disassembly.

One potential design concept that would be simple to assemble is one in which all coils are constrained to lie within toroidal sectors; i.e. in which there are designated planes of constant toroidal angle that no coils cross. To attain a design like this with GSCO, the first step is to impose constraints on a wireframe that prevent current from crossing certain toroidal planes. Such a set of constraints is displayed in Fig. 11. In this schematic, the orange segments are subject to the segment constraints of Eq. 7. Hence, they may not carry any current and, for the purposes of GSCO, a cell that contains one or more of these constrained segments is not eligible for the addition of a loop of current. Note that the constraints here are only applied to *toroidal* segments; hence, it is allowable to

add planar coils within these constrained regions in which the current flows in a strictly *poloidal* direction.

A sample solution that uses these constraints is shown in Fig. 12. The wireframe was initialized with a set of planar, poloidal current flows to produce the required toroidal field. These current flows were placed inside the regions where the poloidal segments were constrained and loops of current could not be added during GSCO; hence, their shapes would remain unchanged. There are only three planar coils per half-period in this example, in contrast to the six used in the modular coil solution in Sec. IV B, although the net poloidal current is the same (5 MA), producing an average field on axis of 1 T.

For the optimization in Sec. IV B, the loop current in GSCO needed to equal the current in the initialized planar coils so that their shapes could be modified by current loops without creating forked current paths. In this case, by contrast, the optimization will not place current loops adjacent to the planar coils. Thus, the choice of loop current is arbitrary. To determine which current level was best suited for this application, multiple optimizations were performed with different loop current levels. In the optimizations performed to date, the best results have been achieved for this configuration with a loop current of 0.15 MA, or 3% of the total poloidal current.

The solution shown in Fig. 12 was run with a loop current of 0.15 MA and $\lambda_S = 10^{-7.5} \text{ T}^2\text{m}^2$. Renderings of the active segments of the final current distribution are rendered in 3D in Fig. 12a and in 2D (for one half-period) in Fig. 12b. For visual clarity, the wireframe segments in the 3D rendering are superimposed on an opaque toroidal surface. The 3D rendering is viewed from above, such that the initialized planar coils appear as straight lines radiating from the center. In the 2D rendering, the planar coils appear as straight, vertical lines. The field created by this current distribution is highly accurate, with $(\mathbf{B} \cdot \hat{\mathbf{n}})/|\mathbf{B}|$ rarely exceeding 1% (Fig. 12c) and with flux surfaces that exhibit excellent agreement with the target plasma boundary (Fig. 12d).

As a result of the constraints placed on the optimization, the saddle coils are conveniently confined to sectors between the planar coils. With this layout, the device would likely be easier and faster to assemble and disassemble for maintenance. From the standpoint of a power plant, any reduction of maintenance time would make the plant more economical.

The current distribution in Fig. 12a-b is substantially less sparse than the modular coil solutions in Figs. 9c-d. However, note that the current paths in this solution tend to appear in concentric loops with like polarities, particularly on the in-board side (Fig. 12b, $100^\circ < \theta_{wf} < 260^\circ$). Thus, rather than interpreting each of these concentric loops as an individual coil, it may be more useful to view the sets of concentric loops as single saddle coils with finite dimensions, with the individual filaments forming the basis for the design of a winding pack.

D. Multiple currents

The solutions presented in the previous sections each utilized a single run of GSCO with fixed values of hyperparam-

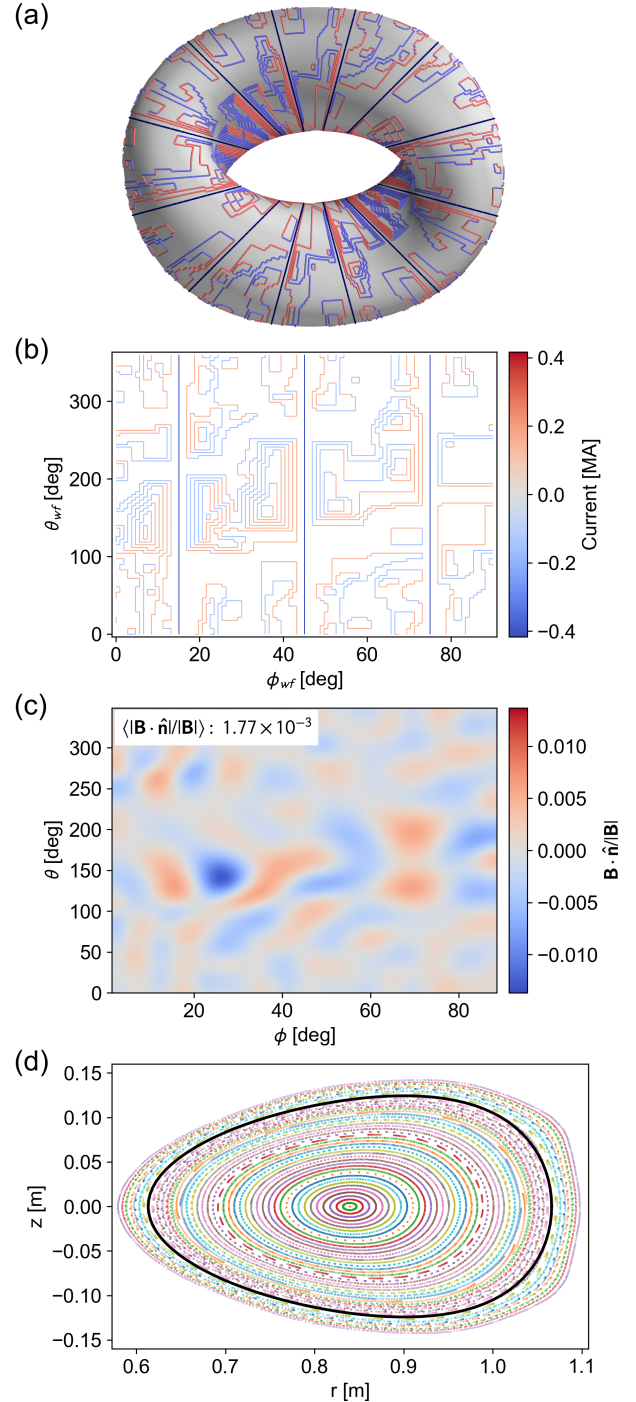


FIG. 12. Current distribution and magnetic field properties of a wireframe containing a set of planar TF coils and saddle coils produced by GSCO constrained to lie within toroidal sectors. (a) 3D rendering of the active segments superimposed, for visual clarity, on a torus that fills the volume of the wireframe; (b) 2D rendering of the currents in one half-period of the wireframe; (c) relative normal component of the magnetic field on one half-period of the target plasma boundary; (d) Poincaré cross-section of field lines produced by the wireframe distribution, with the target plasma boundary shown as the black curve.

eters such as the loop current I_{loop} and weighting factor λ_S . One consequence of this was that all coils constructed by the GSCO algorithm carried the same current. However, it could be advantageous seek solutions in which different coils carry different currents. Such solutions can be attained by performing a sequence of GSCO procedures with varying parameters at each step. One example is shown in Fig. 13, and the associated procedure is summarized in Algorithm 2.

The procedure applied the standard GSCO function (Algorithm 1) multiple times, each time using a different loop current I_{loop} . In this way, the solution obtained a few new coils at each step with a distinct current level. The sequence proceeded in a “drop-down” manner, with the first optimization using the highest current ($I_{\text{loop}} = 1$ MA), and with each subsequent optimization using one-half of the loop current of the previous optimization.

The procedure also took measures to avoid potentially inconvenient features such as concentric coils which had been prevalent in the solution in Sec. IV C, or very small coils. To lessen the likelihood of concentric coils appearing, the each GSCO optimization was run with the “max loops per cell” rule (Table I) with $N_{\text{max}} = 1$. In addition, following each GSCO step, all segments enclosed within existing coils were constrained to carry zero current. To avoid the presence of overly small saddle coils, any coil at the end of an optimization that enclosed fewer than 20 cells was eliminated before starting the subsequent optimization. Presumably, if a very small coil appears in a given region during one optimization in the sequence, a larger coil would be placed in the same location with half the current in the next optimization.

After several sequential GSCO procedures with decreasing loop current levels, a final GSCO procedure was performed to fine-tune the shapes of the existing coils without adding any new coils. Practically, this was accomplished by removing the constraints on segments enclosed by coils and invoking the “no new coils” rule (Table I) with an enhanced version of the original GSCO function that offers the option to match existing currents in the wireframe. This is summarized in Algorithm 3 as the function GSCO_MATCH. The current-matching feature is implemented in each iteration through an additional step performed prior to checking the eligibility of a given cell. Specifically, if the cell contains segments that are already part of an existing coil with a current I_{match} , the optimizer will consider a loop current for that cell with a current equal to I_{match} rather than the default current I_{default} supplied by the user as a hyperparameter. This is advantageous when the initial current distribution x_{init} contains coils with different currents. When the greedy optimizer has the flexibility to add loops of current that match the current of the coils that the loops are next to, the optimizer is able to adjust the shapes of all the coils in a single function call.

Note that if a single cell contains segments utilized by different coils with different current levels, it is also considered ineligible for the addition of a current loop, as the value to use for I_{match} is ambiguous. Furthermore, adding a loop with any (nonzero) value of I_{match} in this case would create a forked current path.

In general, if a given cell has no current-carrying seg-

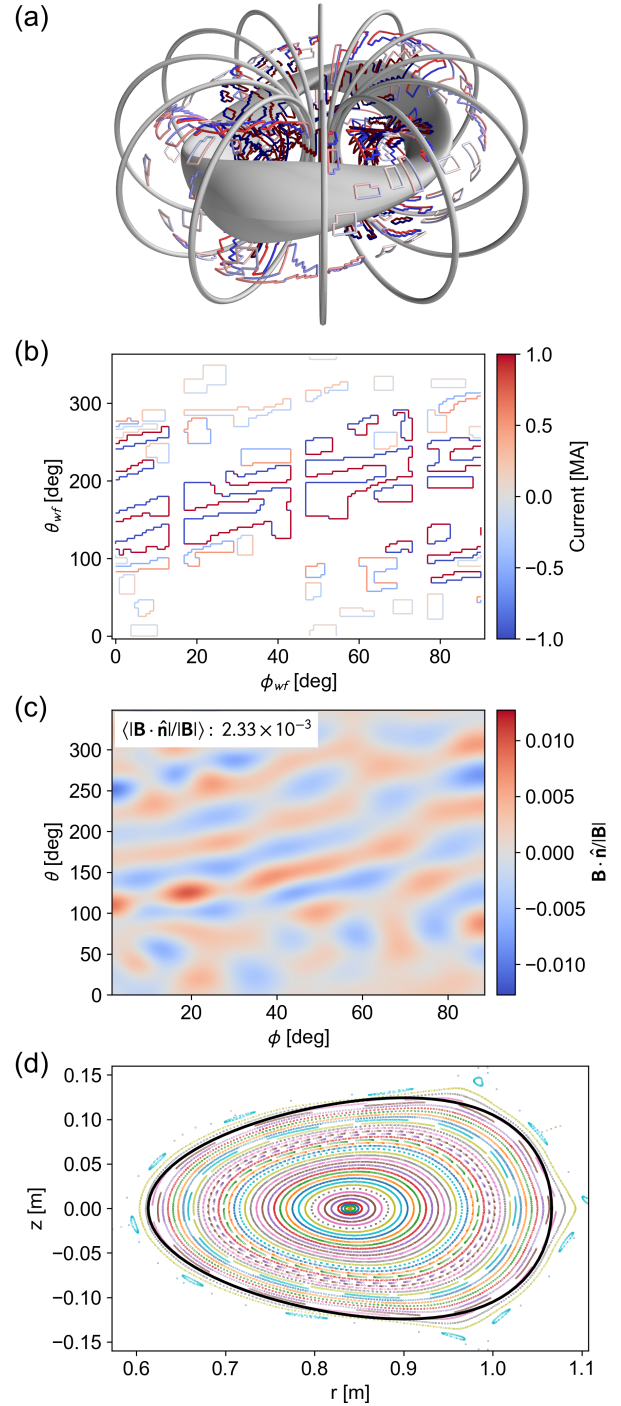


FIG. 13. Current distribution and magnetic field properties of a wireframe with saddle coils designed in a sequence of GSCO procedures. (a) 3D rendering of the active segments along with accompanying circular TF coils and the target plasma boundary; (b) 2D rendering of the currents in one half-period of the wireframe; (c) relative normal component of the magnetic field on one half-period of the target plasma boundary; (d) Poincaré cross-section of field lines produced by the wireframe distribution, with the target plasma boundary shown as the black curve.

Algorithm 2: Multistage GSCO

Input: $\mathbf{A}, \mathbf{b}, \mathbf{C}, \mathbf{d}, \{\mathbf{u}_i | 1 \leq i \leq \# \text{ cells in wireframe}\}$
Output: Optimized wireframe currents (\mathbf{x})
function GSCO_MULTISTAGE($\mathbf{x}_{\text{init}}, I_{\text{start}}, \lambda_S, N_{\text{cells}, \text{min}}$)
 RULES1 = {wireframe constraints, no crossing, max loops per cell (1)}
 $\mathbf{x} = \mathbf{x}_{\text{init}}$
 $I_{\text{loop}} = I_{\text{start}}$
repeat
 $\mathbf{x} = \text{GSCO}(\mathbf{x}, I_{\text{loop}}, \lambda_S, \text{RULES1})$
 Remove coils from \mathbf{x} enclosing fewer cells than $N_{\text{cells}, \text{min}}$
 Update \mathbf{C} and \mathbf{d} to constrain segments within new coils to carry no current
 $I_{\text{loop}} = I_{\text{loop}}/2$
until \mathbf{x} does not change from previous iteration
 Update \mathbf{C} and \mathbf{d} to remove constraints on segments within coils
 RULES2 = RULES1 \cup {no new coils}
 $\mathbf{x} = \text{GSCO_MATCH}(\mathbf{x}, 0, \lambda_S, \text{RULES2})$
return \mathbf{x}
end

Algorithm 3: GSCO with current matching

Input: $\mathbf{A}, \mathbf{b}, \mathbf{C}, \mathbf{d}, \{\mathbf{u}_i | 1 \leq i \leq \# \text{ cells in wireframe}\}$
Output: Optimized wireframe currents (\mathbf{x})
function GSCO_MATCH($\mathbf{x}_{\text{init}}, I_{\text{default}}, \lambda_S, \text{RULES}$)
 $\mathbf{x} = \mathbf{x}_{\text{init}}$
repeat
 $L = \{\}$
 for $i = 1, \dots, \# \text{ cells in wireframe}$ **do**
 $\{I_j | 1 \leq j \leq 4\}$ = the currents in the segments around cell i
 if $I_j = 0$ for all j **then**
 $I_{\text{loop}} = I_{\text{default}}$
 end
 else if the nonzero I_j have a single absolute value ($\equiv I_{\text{match}}$) **then**
 $I_{\text{loop}} = I_{\text{match}}$
 end
 else
 Not eligible; continue to next cell
 end
 if $\mathbf{x} + I_{\text{loop}}\mathbf{u}_i$ obeys all RULES **then**
 $L = L \cup \{I_{\text{loop}}\mathbf{u}_i\}$
 end
 if $\mathbf{x} - I_{\text{loop}}\mathbf{u}_i$ obeys all RULES **then**
 $L = L \cup \{-I_{\text{loop}}\mathbf{u}_i\}$
 end
 end
 $\mathbf{y}^* = \min_{\mathbf{y} \in L} [f_B(\mathbf{x} + \mathbf{y}) + \lambda_S f_S(\mathbf{x} + \mathbf{y})]$
 $\mathbf{x} = \mathbf{x} + \mathbf{y}^*$
until no eligible cells exist or f_{GSCO} stops decreasing
return \mathbf{x}
end

ments (i.e., the cell is not adjacent to an existing coil), GSCO_MATCH can consider adding a loop of current with a user-specified default current level. However, for the application in the multistage GSCO procedure (Algorithm 2), this feature was circumvented by applying the “no new coils” rule and (redundantly) setting the I_{default} hyperparameter to 0. This is done because the goal at this final step of Algorithm 2 is strictly to refine the shapes of the existing coils rather than to add any new ones.

Applying the multistage procedure (Algorithm 2) to a wireframe around the Precise QA equilibrium yielded the solution shown in Fig. 13a-b. Similarly to solution in Sec. IV C, the saddle coils added by the GSCO procedures are confined to toroidal sectors. One new aspect of this solution is that the toroidal field is produced not by the wireframe itself but by a set of external, circular TF (toroidal field) coils. Therefore, the wireframe was not initialized with any poloidal current flows. Hence, this solution demonstrates how a wireframe can be optimized to improve the field created by a pre-existing set of coils.

The multistage procedure used $\lambda_S = 1 \times 10^{-7} \text{ T}^2\text{m}^2$. The starting loop current I_{start} was 1 MA. Ultimately, the successive applications of GSCO added coils with currents of 1 MA, 500 kA, 250 kA, 125 kA, and 62.5 kA; subsequent GSCO runs with lower currents failed to add any coils above the minimum size $N_{\text{cells}, \text{min}}$. The computation time to perform Algorithm 2 for this solution was substantially lower than the time required to perform Algorithm 1 for the solutions in Sec. IV B and IV C. This is due to the more stringent constraints used in each optimization, which greatly reduced the number of eligible cells for the optimizer to check during each iteration. Using 4 cores on a 2.9 GHz Intel Cascade Lake processor node on the Stellar cluster, the longest call to GSCO in the sequence took 34 seconds, or 136 CPU-seconds. Running the entire procedure on a laptop, including additional steps for setting up the wireframe and post-processing, took less than 5 minutes.

Remarkably, the solution leaves a substantial amount of empty space on the outboard side, particularly for $\theta_{wf} < 100^\circ$ and $15^\circ < \phi_{wf} < 45^\circ$ in Fig. 13b. This is the case despite no specific spatial restrictions having been placed on this area. Nevertheless, the field accuracy is quite good, with $(\mathbf{B} \cdot \hat{\mathbf{n}})/|\mathbf{B}|$ is mostly below 1% (13c). The field exhibits decent flux surface agreement (Fig. 13d), although the flux surfaces near the plasma boundary appear to be deformed slightly by a resonant perturbation just outside. Field accuracy could be improved by running the optimization with a lower value of λ_S , although this would come at the expense of adding more coils with more complicated geometry.

V. SUMMARY AND CONCLUSIONS

In this paper, the wireframe framework for stellarator coil design and optimization was introduced. Consisting of a set of interconnected current-carrying segments, the wireframe offers a solution space with a spatially local parametrization that enables the imposition of arbitrary constraints on where

current flows may be located. Two methods of optimizing the wireframe segment currents were introduced: Regularized Constrained Least Squares (RCLS) and Greedy Stellarator Coil Optimization (GSCO).

RCLS is a rapid, linear optimizer that can produce highly accurate solutions on coarse grids, although the prevalence of junctions of segments that each have unique current levels could make these distributions difficult to realize in practice.

GSCO is a fully discrete algorithm that can construct flows of current in the wireframe that avoid the complicated current junctions seen in the RCLS solutions and control the number of unique current levels required to implement the solution. GSCO is also topologically flexible and can both add new coils and reshape pre-existing coils in a single optimization. As demonstrated in Sec. IV, it could produce both modular coil solutions and saddle coil solutions for the same target plasma equilibrium, with the nature of the solution dependent on the initialization and constraints imposed.

The example solutions for both optimization methods illustrated the ease with which arbitrary spatial constraints may be placed on current distributions. Since the current distribution is parametrized according to the current carried by each individual segment, such spatial constraints can be implemented simply by zeroing out the parameters corresponding to any subset of segments where current flow is not desired. For example, current distributions can be constrained to leave space for ports (Fig. 5), or to keep current flows confined to predefined toroidal sectors for ease of assembly (Figs. 12 and 13).

While the current flow patterns in the GSCO solutions cannot themselves constitute designs for coils due to their filamentary nature and the sharp corners at the wireframe nodes, they can serve as a starting point for coil geometry that can be subsequently refined with space curve optimization techniques. The value of the GSCO procedure in this case lies in its ability to:

1. identify the most important locations for saddle coils and/or shape modifications for pre-existing coils,
2. determine coil shapes within the wireframe solution space that produce a highly accurate field,
3. obey spatial constraints that would be more difficult to enforce with other optimization methods, and
4. exhibit flexibility in determining the number of coils.

There are many possibilities for expanding the wireframe framework and associated optimization methods to increase flexibility and access larger solution spaces. For example, with the GSCO procedure, many solutions can only be found through optimization in multiple stages that use different hyperparameters, as was the case for the multi-current solution in Sec. IVD. By further developing customized recipes for GSCO sequences, it should be possible to find solutions that are better suited for a variety of applications and device requirements.

In addition, there are ways of generalizing the wireframe itself that may lead to better solutions. For one, it may be worth experimenting with different segment meshing structures (e.g.

triangles). Furthermore, all of the wireframes utilized in this paper exhibited two-dimensional, toroidal topology, and were thus analogous to the toroidal winding surfaces used in many existing coil design techniques. The use of this type of wireframe effectively constrains the optimized current distribution to exist on a pre-specified surface, which puts strict limits the solution space. However, in principle, wireframes can be constructed with three-dimensional topology, with segments filling a volume around the plasma and thus enabling a much more extensive solution space. Such wireframes will be developed and investigated as next steps.

VI. ACKNOWLEDGMENTS

The research described in this paper was conducted under the Laboratory Directed Research and Development (LDRD) Program at the Princeton Plasma Physics Laboratory, a national laboratory operated by Princeton University for the U.S. Department of Energy under Prime Contract No. DE-AC02-09CH11466. The United States Government retains a non-exclusive, paid-up, irrevocable, world-wide license to publish or reproduce the published form of this manuscript, or allow others to do so, for United States Government purposes.

VII. DATA AND CODE AVAILABILITY

The methods developed for this paper are implemented in the open-source SIMSOPT codebase [46]. The three-dimensional plots were rendered with the Mayavi scientific visualization package [47]. The data presented here, along with scripts for reproducing the key results, are available at <https://doi.org/10.34770/6pbm-9981>.

Appendix A: Derivation of the formula for the magnetic field from a straight wire segment

The formula in Eq. 1 for the magnetic field generated by a straight segment of wire may be derived from the Biot-Savart law for the magnetic field from a general space curve. The segment formula is sometimes utilized to calculate the field from filamentary coils in which space curves are approximated as polygons. This approach is taken, for example, by the FLARE code [48] and by the MAKEGRID code in the STELLOPT codebase [49]. Derivations using alternate approaches may be found in Refs. [30] and [31].

To compute the expression for the magnetic field \mathbf{B} at an evaluation point \mathbf{p}_o from a current I flowing in a segment of wire from point \mathbf{p}_1 to point \mathbf{p}_2 , one begins with the Biot-Savart integral:

$$\mathbf{B} = \frac{\mu_0}{4\pi} \int_{\mathbf{p}_1}^{\mathbf{p}_2} \frac{I d\mathbf{l}' \times \mathbf{r}'}{|\mathbf{r}'|^3} \quad (\text{A1})$$

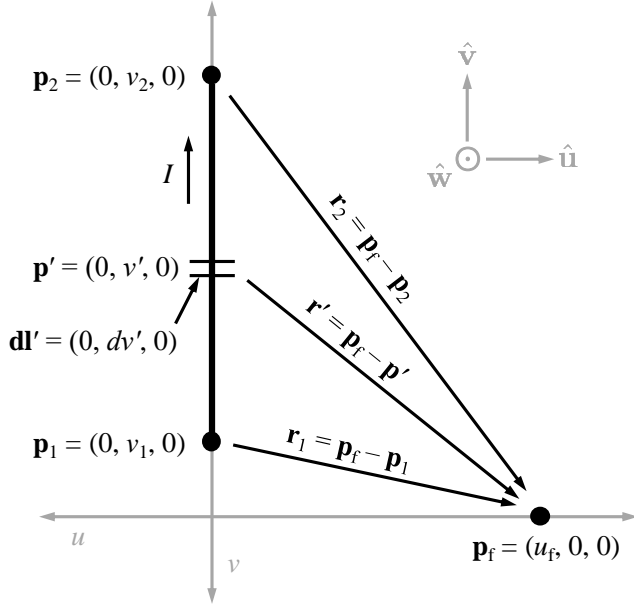


FIG. 14. Setup for the computation of the Biot-Savart integral over a straight segment of wire.

Here, \mathbf{dl}' is a differential element of the wire segment and \mathbf{r}' is a vector from the differential element to the field evaluation point \mathbf{p}_f .

To compute the integral, the wireframe and test point will be placed in the coordinate system (u, v, w) shown in Fig. 14. The evaluation point lies on the u axis at the point $(u_f, 0, 0)$ and the segment is positioned on the v axis between the points $(0, v_1, 0)$ and $(0, v_2, 0)$. The differential interval \mathbf{dl}' along the segment is $(0, dv', 0)$. The vector \mathbf{r}' is then $(u_f, 0, 0) - (0, v', 0) = (u_f, -v', 0)$ and

$$\begin{aligned} \mathbf{dl}' \times \mathbf{r}' &= (0, 0, -u_f dv') \\ &= -u_f dv' \hat{\mathbf{w}} \end{aligned} \quad (\text{A2})$$

Here, $\hat{\mathbf{w}}$ is a unit vector perpendicular to the plane containing the segment and the evaluation point (defined more precisely below).

The integral may then be written as

$$\mathbf{B} = -\frac{\mu_0 I}{4\pi} \hat{\mathbf{w}} \int_{v_1}^{v_2} \frac{u_f}{(u_f^2 + v'^2)^{3/2}} dv' \quad (\text{A3})$$

and evaluates to

$$\mathbf{B} = -\frac{\mu_0 I}{4\pi} \left(\frac{1}{u_f} \right) \left(\frac{v_2}{\sqrt{u_f^2 + v_2^2}} - \frac{v_1}{\sqrt{u_f^2 + v_1^2}} \right) \hat{\mathbf{w}} \quad (\text{A4})$$

The expression in Eq. A4 may be rewritten in coordinate-free form by noting the following. First, the unit vectors $\hat{\mathbf{u}}$, $\hat{\mathbf{v}}$, and $\hat{\mathbf{w}}$ can be expressed in terms of \mathbf{r}_1 and \mathbf{r}_2 as

$$\hat{\mathbf{w}} = \frac{\mathbf{r}_2 \times \mathbf{r}_1}{|\mathbf{r}_2 \times \mathbf{r}_1|} \quad (\text{A5})$$

$$\hat{\mathbf{v}} = \frac{\mathbf{r}_1 - \mathbf{r}_2}{|\mathbf{r}_1 - \mathbf{r}_2|} \quad (\text{A6})$$

$$\hat{\mathbf{u}} = \hat{\mathbf{v}} \times \hat{\mathbf{w}} = \frac{(|\mathbf{r}_2|^2 - \mathbf{r}_1 \cdot \mathbf{r}_2) \mathbf{r}_1 + (|\mathbf{r}_1|^2 - \mathbf{r}_1 \cdot \mathbf{r}_2) \mathbf{r}_2}{|\mathbf{r}_1 - \mathbf{r}_2| |\mathbf{r}_1 \times \mathbf{r}_2|} \quad (\text{A7})$$

Using Equations (A5) to (A7), the coordinates v_1 , v_2 , and u_f may be written as

$$v_1 = -\mathbf{r}_1 \cdot \hat{\mathbf{v}} = \frac{\mathbf{r}_1 \cdot \mathbf{r}_2 - |\mathbf{r}_1|^2}{|\mathbf{r}_1 - \mathbf{r}_2|} \quad (\text{A8})$$

$$v_2 = -\mathbf{r}_2 \cdot \hat{\mathbf{v}} = \frac{|\mathbf{r}_2|^2 - \mathbf{r}_1 \cdot \mathbf{r}_2}{|\mathbf{r}_1 - \mathbf{r}_2|} \quad (\text{A9})$$

$$u_f = \mathbf{r}_1 \cdot \hat{\mathbf{u}} = \frac{|\mathbf{r}_1|^2 |\mathbf{r}_2|^2 - (\mathbf{r}_1 \cdot \mathbf{r}_2)^2}{|\mathbf{r}_1 - \mathbf{r}_2| |\mathbf{r}_1 \times \mathbf{r}_2|} = \frac{|\mathbf{r}_1 \times \mathbf{r}_2|}{|\mathbf{r}_1 - \mathbf{r}_2|} \quad (\text{A10})$$

Finally, substituting Equations (A5) and (A8) to (A10) into Equation (A4), also noting that $\sqrt{u_f^2 + v_1^2} = |\mathbf{r}_1|$ and $\sqrt{u_f^2 + v_2^2} = |\mathbf{r}_2|$, yields, after some algebra, the expression in Eq. 1:

$$\mathbf{B} = \frac{\mu_0 I}{4\pi} \left(\frac{|\mathbf{r}_1| + |\mathbf{r}_2|}{|\mathbf{r}_1| |\mathbf{r}_2| (|\mathbf{r}_1| |\mathbf{r}_2| + \mathbf{r}_1 \cdot \mathbf{r}_2)} \right) \mathbf{r}_1 \times \mathbf{r}_2 \quad (\text{A11})$$

The expression is mathematically valid for any point that does not lie on the segment between \mathbf{p}_1 and \mathbf{p}_2 , in which case the term $|\mathbf{r}_1| |\mathbf{r}_2| + \mathbf{r}_1 \cdot \mathbf{r}_2$ in the denominator is zero. This situation should not arise in practical wireframe applications, however, as the magnetic field of interest is located on the plasma boundary, which is assumed not to intersect any wireframe segment.

In general, using a filamentary approximation for a wire with finite thickness introduces an error in the magnetic field calculation proportional to $(t/d)^2$, where t is the thickness of the wire and d is the distance from the wire to the field evaluation point [15]. In principle, this error could be reduced with a more sophisticated model for the wireframe in which each segment has a finite thickness and the junction geometry at the nodes is implemented carefully such that the continuity constraint equations (Eq. 4) still prevent charge accumulation. However, related to the discussion Sec. IV A, even with finite segment build, the wireframe current distribution is unlikely to resemble a final coil design. Rather, the wireframe current distribution would need to be refined such that the current flows take smoother paths. It may more worthwhile to account for finite thickness in this subsequent refining stage rather than during the optimization of the wireframe currents.

Appendix B: Derivation of the equations for RCLS

The RCLS problem in Eq. 15 constitutes a linear least-squares minimization subject to linear equality constraints and a regularization term. The first step in solving the problem is to represent the solution space for \mathbf{x} in a basis in which its components are either fully determined by the constraints (i.e. in the image of the constraint matrix) or completely unconstrained (i.e. in the null space of the constraint matrix). As described, for example, in Ref. [50] (Section 3.4) or [51], this can be done by computing the “full” QR factorization of the transpose of the constraint matrix \mathbf{C}^T :

$$\mathbf{C}^T = [\mathbf{Q} \ \tilde{\mathbf{Q}}] \begin{bmatrix} \mathbf{R} \\ 0 \end{bmatrix} \quad (\text{B1})$$

Here, $\mathbf{C} \in \mathbb{R}^{p \times n}$ is the constraint matrix as defined in Eq. 8, n is the number of elements in \mathbf{x} (the number of wireframe segments), and p is the number of linearly independent constraint equations. The p columns of submatrix $\mathbf{Q} \in \mathbb{R}^{n \times p}$ and the $n - p$ columns of $\tilde{\mathbf{Q}} \in \mathbb{R}^{n \times (n-p)}$ are orthonormal unit vectors, and $\mathbf{R} \in \mathbb{R}^{(n-p) \times (n-p)}$ is an upper triangular matrix.

Now define vectors $\mathbf{u} \in \mathbb{R}^p$ and $\mathbf{v} \in \mathbb{R}^{n-p}$ in the bases specified by the columns of \mathbf{Q} and $\tilde{\mathbf{Q}}$:

$$\begin{bmatrix} \mathbf{Q}^T \\ \tilde{\mathbf{Q}}^T \end{bmatrix} \mathbf{x} = \begin{bmatrix} \mathbf{u} \\ \mathbf{v} \end{bmatrix} \quad (\text{B2})$$

Using the orthogonality property of the matrix on the left-hand side of Eq. B2, \mathbf{x} may be written in terms of \mathbf{u} and \mathbf{v} as

$$\mathbf{x} = [\mathbf{Q} \ \tilde{\mathbf{Q}}] \begin{bmatrix} \mathbf{u} \\ \mathbf{v} \end{bmatrix} = \mathbf{Q}\mathbf{u} + \tilde{\mathbf{Q}}\mathbf{v} \quad (\text{B3})$$

Using Eq. B3, Eq. 16 can be expressed as

$$\mathbf{R}^T \mathbf{Q}^T \mathbf{x} = \mathbf{d}, \quad (\text{B4})$$

or, after incorporating Eq. B2,

$$\mathbf{R}^T \mathbf{u} = \mathbf{d} \quad (\text{B5})$$

Thus, the constraints fix the vector \mathbf{u} whereas \mathbf{v} represents the part of the solution that is unrestricted by the constraints. Eq. B5 can be solved efficiently for \mathbf{u} using forward substitution, as \mathbf{R}^T is lower triangular.

With \mathbf{u} now known, it remains to determine \mathbf{v} , the unconstrained part of the solution. Using Eq. B3, the total objective function f may be written as

$$f = \frac{1}{2} (\mathbf{A}\mathbf{Q}\mathbf{u} + \mathbf{A}\tilde{\mathbf{Q}}\mathbf{v} - \mathbf{b})^2 + \frac{1}{2} (\mathbf{W}\mathbf{Q}\mathbf{u} + \mathbf{W}\tilde{\mathbf{Q}}\mathbf{v})^2 \quad (\text{B6})$$

The least-squares solution \mathbf{v}^* that minimizes f is that which causes the gradient of f to vanish:

$$\nabla_{\mathbf{v}} f = \tilde{\mathbf{Q}}^T \mathbf{A}^T (\mathbf{A}\mathbf{Q}\mathbf{u} + \mathbf{A}\tilde{\mathbf{Q}}\mathbf{v} - \mathbf{b}) + \tilde{\mathbf{Q}}^T \mathbf{W}^T (\mathbf{W}\mathbf{Q}\mathbf{u} + \mathbf{W}\tilde{\mathbf{Q}}\mathbf{v}) = 0 \quad (\text{B7})$$

Collecting like terms and rearranging leads to

$$\tilde{\mathbf{Q}}^T (\mathbf{A}^T \mathbf{A} \tilde{\mathbf{Q}} + \mathbf{W}^T \mathbf{W} \tilde{\mathbf{Q}}) \mathbf{v} = \tilde{\mathbf{Q}}^T (\mathbf{A}^T \mathbf{b} - \mathbf{A}^T \mathbf{A} \mathbf{Q} - \mathbf{W}^T \mathbf{W} \mathbf{Q}) \mathbf{u} \quad (\text{B8})$$

Eq. B8 constitutes a system of linear equations that can then be solved directly for \mathbf{v} . Along with the solution for \mathbf{u} determined in Eq. B5, the solution \mathbf{x}^* to the constrained least squares problem can then be computed via Eq. B3.

For high-resolution wireframes, in which the matrices \mathbf{A} and \mathbf{W} are large, the problem may be difficult to solve directly due to memory constraints and poor matrix conditioning. In this case, iterative algorithms with preconditioners may be employed. Similar high-dimensional constrained linear least squares problems have been solved with such techniques, for example, in Ref. [26].

Appendix C: Dependence of GSCO solutions on wireframe geometry

In each optimization shown in this paper, the free parameters were the currents in each segment of the underlying wireframe. The positions, lengths, and connectivity of the wireframe segments were held fixed during the optimizations. However, these geometric aspects naturally influence the ability of the optimizer to find an accurate solution. To get an indication of the sensitivity of the solutions to the geometry of the wireframe, a GSCO procedure was run on two wireframes with slight geometric differences.

The first test wireframe was used for the optimizations performed in Sec. IV. It was created by first generating a toroidal surface offset roughly 30 cm from the target plasma boundary. This surface was calculated by the BNORM code. BNORM was originally developed to prepare winding surfaces and calculate the target normal field on the plasma boundary for NESCOIL computations [5], and is currently available in the STELLOPT code suite [49]. Its method for generating offset surfaces is described in Appendix B of Ref. [2].

The offset surface geometry is parametrized with a toroidal angle ζ and a poloidal angle θ . The toroidal angle ζ coincides with the standard azimuthal angle ϕ in cylindrical coordinates. The cylindrical radial (r) and vertical (z) coordinates of a point on the surface may be computed for a given θ and ζ .

With this surface generated, the nodes of the wireframe were positioned on the surface on a two-dimensional grid of evenly-spaced intervals of ζ and θ . The resolution of the grid was 96×100 , meaning 96 nodes per half-period in the toroidal dimension and 100 nodes in the poloidal dimension. Because of the equivalence of ζ with the cylindrical azimuthal angle ϕ mentioned above, nodes with a given value of ζ all lie in a plane with the azimuthal angle $\phi = \zeta$. However, in the poloidal dimension, the physical spacing between the nodes is, in general, not regular.

Following the creation of the first wireframe, a second wireframe was generated with slightly different geometry. The nodes were placed on the same toroidal surface at the same azimuthal angles $\phi = \zeta$ and had the same grid resolution of 96×100 ; however, the poloidal intervals between each set of nodes were adjusted such that, for any given ζ , the Euclidean distances between nodes with adjacent θ values were uniform. As a result, each segment in the second wireframe had a slightly different position and orientation than the corresponding segment in the first wireframe with the same toroidal and poloidal index. Similarly, a given current in a particular segment of the second wireframe would have a slightly different contribution to the magnetic field than the same current in the corresponding segment of the first wireframe; in other words, the elements of the matrix \mathbf{A} (Eq. 11) would be different.

Both of these wireframes were initialized with six planar poloidal current flows per half-period at identical toroidal angles. A GSCO procedure was then run on each of the initialized wireframes. Both optimizations used the same hyperparameters, including $\lambda_S = 10^{-6} \text{ T}^2\text{m}^2$ and a loop current equal to the current in the initial poloidal flows.

A comparison of the solutions and their field accuracies is shown in Fig. 15. In Fig. 15a, the active segments from both solutions are overlain. The solution on the wireframe with the original geometry is shown in magenta, whereas the solution on the wireframe with equalized poloidal segment lengths is shown in cyan. Both solutions consist mostly of modular coils, similar to the solutions in Sec. IV B (in fact, the original solution is the solution from Sec. IV B with $\lambda_S = 10^{-6} \text{ T}^2\text{m}^2$). Overall, the modular coils follow qualitatively similar paths, especially on the outboard side. However, some differences in geometry can be seen on the inboard side. These differences are partly due to the different orientations of the segments in each wireframe; in some areas, it is clear that the segments from the modified wireframe are tilted at a substantial angle relative to the segments in the original wireframe.

Overall, both solutions had very similar field accuracy metrics. The mean relative normal field $\langle |\mathbf{B} \cdot \hat{\mathbf{n}}|/|\mathbf{B}| \rangle$ was 2.44×10^{-3} for the solution on the original wireframe, while the solution on the new wireframe had a slightly lower value of $\langle |\mathbf{B} \cdot \hat{\mathbf{n}}|/|\mathbf{B}| \rangle = 2.18 \times 10^{-3}$. However, the flux surfaces created by each solution have more notable differences, as shown in the Poincaré cross-sections in Fig. 15b for the original wireframe geometry and Fig. 15c for the modified wireframe geometry. Even though the solution on the modified wireframe had a slightly better summary field accuracy metric $\langle |\mathbf{B} \cdot \hat{\mathbf{n}}|/|\mathbf{B}| \rangle$, it appears to be impacted by a resonant field error that deforms the flux surface geometry near the target plasma boundary.

It is well understood that even a small error field can substantially deform or otherwise impact flux surface geometry in the vicinity of a surface with a rotational transform value that is resonant with the error field [52]. Thus, it is not unexpected that small changes in the wireframe geometry might result in a field error that is small but large enough to impact the flux surfaces.

It is not ideal that the achievable flux surface quality of GSCO solutions can be so sensitive to small changes in the geometry of the underlying wireframe. However, it is hypothesized that there is room for improvement in this regard. For example, while the objective function f_{GSCO} employed in these optimizations includes a general metric of field accuracy, it does not include specific, elevated penalties for resonant error fields. If such a penalty were added, it might be possible to achieve a better solution with the second wireframe. Alternatively, if the solution on the second wireframe is refined with a space curve optimizer, this subsequent optimization could use a resonant error objective in order to heal the resonant error field. In the meantime, when developing wireframe solutions for a given plasma equilibrium, it is generally good practice to repeat optimizations with slight variations in wireframe geometry to see if better solutions are achievable.

-
- [1] L.-M. Imbert-Gérard, E. J. Paul, and A. M. Wright, *An Introduction to Stellarators: from magnetic fields to symmetries and optimization* (Society for Industrial and Applied Mathematics, Philadelphia, PA, 2025).
 - [2] M. Landreman, An improved current potential method for fast computation of stellarator coil shapes, *Nuclear Fusion* **57**, 046003 (2017).
 - [3] P. Helander, M. Drevlak, M. Zarnstorff, and S. C. Cowley, Stellarators with permanent magnets, *Physical Review Letters* **124**, 095001 (2020).
 - [4] L. Bromberg, M. Zarnstorff, O. Meneghini, T. Brown, P. Heitzenroeder, G. H. Neilson, J. V. Minervini, and A. Boozer, Stellarator configuration improvement using high temperature superconducting monoliths, *Fusion Science and Technology* **60**, 643 (2011).
 - [5] P. Merkel, Solution of stellarator boundary value problems with external currents, *Nuclear Fusion* **27**, 867 (1987).
 - [6] M. Drevlak, Automated optimization of stellarator coils, *Fusion Technology* **33**, 106 (1998).
 - [7] W. H. Miner, P. M. Valanju, S. P. Hirshman, A. Brooks, and N. Pomphrey, Use of a genetic algorithm for compact stellarator design, *Nuclear Fusion* **41**, 1185 (2000).
 - [8] E. J. Paul, M. Landreman, A. Bader, and W. Dorland, An adjoint method for gradient-based optimization of stellarator coil shapes, *Nuclear Fusion* **58**, 076015 (2018).
 - [9] D. J. Strickler, L. A. Berry, and S. P. Hirshman, Designing coils for compact stellarators, *Fusion Science and Technology* **41**, 107 (2022).
 - [10] C. Zhu, S. R. Hudson, Y. Song, and Y. Wan, New method to design stellarator coils without the winding surface, *Nuclear Fusion* **58**, 016008 (2018).
 - [11] T. Brown, J. Breslau, D. Gates, N. Pomphrey, and A. Zolfaghari, Engineering optimization of stellarator coils lead to improvements in device maintenance, in *26th IEEE Symposium on Fusion Engineering (SOFE)* (2015).
 - [12] H. Yamaguchi, S. Satake, M. Nakata, A. Shimizu, Y. Suzuki, and the W7-X team, Optimization of modular and helical coils applying genetic algorithm and fully-three-dimensional B-

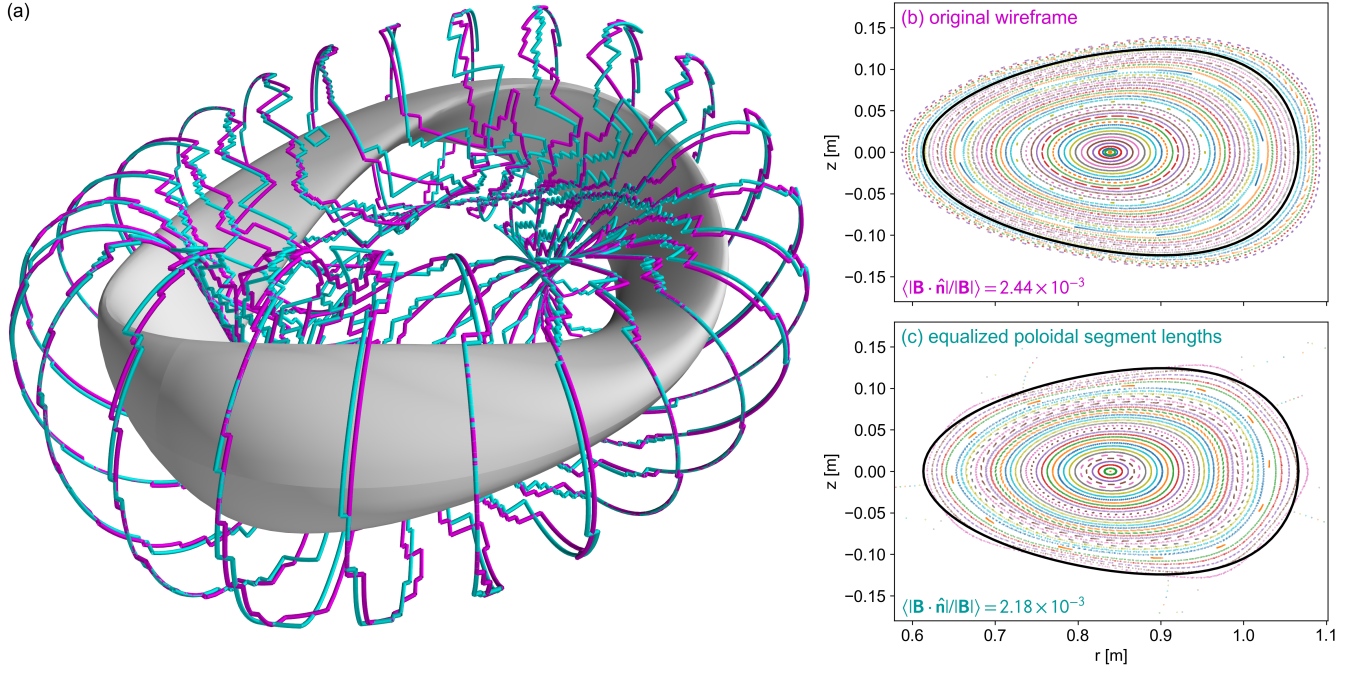


FIG. 15. Comparison of GSCO solutions performed with the same hyperparameters on wireframes with the same grid resolution but slightly different segment geometry. (a) Rendering of the active segments from the solution with the original wireframe (magenta) and the wireframe with adjusted poloidal segment lengths (cyan), along with the target plasma boundary; (b-c) Poincaré cross-sections of field lines traced for each solution alongside the cross-section of the target plasma boundary.

- spline curves, *Nuclear Fusion* **61**, 106004 (2021).
- [13] N. Lonigro and C. Zhu, Stellarator coil design using cubic splines for improved access to the outboard side, *Nuclear Fusion* **62**, 066009 (2022).
 - [14] L. Singh, T. G. Kruger, A. Bader, C. Zhu, S. R. Hudson, and D. T. Anderson, Optimization of finite-build stellarator coils, *Journal of Plasma Physics* **86**, 905860404 (2020).
 - [15] N. McGreivy, S. R. Hudson, and C. Zhu, Optimized finite-build stellarator coils using automatic differentiation, *Nuclear Fusion* **61**, 026020 (2021).
 - [16] C. Zhu, M. Zarnstorff, D. Gates, and A. Brooks, Designing stellarators using perpendicular permanent magnets, *Nuclear Fusion* **60**, 076016 (2020).
 - [17] M. Landreman and C. Zhu, Calculation of permanent magnet arrangements for stellarators: a linear least-squares method, *Plasma Physics and Controlled Fusion* **63**, 035001 (2021).
 - [18] G. S. Xu, Z. Y. Lu, D. H. Chen, L. Chen, X. Y. Zhang, X. Q. Wu, M. Y. Ye, and B. N. Wan, Design of quasi-axisymmetric stellarators with varying-thickness permanent magnets based on Fourier and surface magnetic charges method, *Nuclear Fusion* **61**, 026025 (2021).
 - [19] C. Zhu, K. C. Hammond, M. Zarnstorff, T. Brown, D. Gates, K. Corrigan, M. Sibilis, and E. Feibush, Topology optimization of permanent magnets for stellarators, *Nuclear Fusion* **60**, 106002 (2020).
 - [20] A. A. Kaptanoglu, T. Qian, F. Wechsung, and M. Landreman, Permanent magnet optimization for stellarators as sparse regression, *Physical Review Applied* **18**, 044006 (2022).
 - [21] K. C. Hammond, C. Zhu, K. Corrigan, D. A. Gates, R. Lown, R. Mercurio, T. M. Qian, and M. C. Zarnstorff, Design of an arrangement of cubic magnets for a quasi-axisymmetric stellarator experiment, *Nuclear Fusion* **62**, 126065 (2022).
 - [22] T. M. Qian, X. Chu, C. Pagano, D. Patch, M. C. Zarnstorff, B. Berlinger, D. Bishop, A. Chambliss, M. Haque, D. Seidita, and C. Zhu, Design and construction of the MUSE permanent magnet stellarator, *Journal of Plasma Physics* **89**, 955890502 (2023).
 - [23] M. Madeira and R. Jorge, Tokamak to stellarator conversion using permanent magnets, *Plasma Physics and Controlled Fusion* **66**, 085008 (2024).
 - [24] Z. Y. Lu, G. S. Xu, D. H. Chen, L. Chen, X. Y. Zhang, M. Y. Ye, and B. N. Wan, Design of quasi-axisymmetric stellarators with variable-thickness perpendicular permanent magnets based on a two-step magnet design strategy, *Nuclear Fusion* **61**, 106028 (2021).
 - [25] Z. Y. Lu, G. S. Xu, D. H. Chen, X. Y. Zhang, L. Chen, M. Y. Ye, H. Y. Guo, and B. N. Wan, Development of advanced stellarator with identical permanent magnet blocks, *Cell Reports Physical Science* **3**, 100709 (2022).
 - [26] A. A. Kaptanoglu, R. Conlin, and M. Landreman, Greedy permanent magnet optimization, *Nuclear Fusion* **63**, 036016 (2023).
 - [27] K. C. Hammond and A. A. Kaptanoglu, Improved stellarator permanent magnet designs through combined discrete and continuous optimizations, *Computer Physics Communications* **299**, 109127 (2024).
 - [28] T. Elder and A. H. Boozer, Current potential patches, *Physics of Plasmas* **31**, 102501 (2024).
 - [29] A. A. Kaptanoglu, G. P. Langlois, and M. Landreman, Topology optimization for inverse magnetostatics as sparse regression: Application to electromagnetic coils for stellarators, *Computer Methods in Applied Mechanics and Engineering* **418**, 116504 (2024).

- (2024).
- [30] D. V. Anderson, J. Breazeal, C. H. Finan, and B. M. Johnston, *ABXYZ: vector potential (A) and magnetic field (B) code (C) for Cartesian (XYZ) geometry using general current elements*, Tech. Rep. UCRL-52029 (Lawrence Livermore National Laboratory, 1976).
 - [31] J. D. Hanson and S. P. Hirshman, Compact expressions for the Biot-Savart fields of a filamentary segment, *Physics of Plasmas* **9**, 4410 (2002).
 - [32] A. N. Tikhonov, The solution of ill-posed problems and the regularization method, *Proceedings of the USSR Academy of Sciences* **151**, 501 (1963).
 - [33] A. N. Tikhonov, A. V. Goncharsky, V. V. Stepanov, and A. G. Yagola, *Numerical methods for the solution of ill-posed problems* (Springer, 1995).
 - [34] M. Landreman and E. Paul, Magnetic fields with precise quasisymmetry for plasma confinement, *Physical Review Letters* **128**, 035001 (2022).
 - [35] R. L. Dewar and S. R. Hudson, Stellarator symmetry, *Physica D* **112**, 275 (1998).
 - [36] A. V. Aho, J. E. Hopcroft, and J. D. Ullman, *Data Structures and Algorithms* (Addison-Wesley, 1983).
 - [37] Y. C. Pati, R. Rezaiifar, and P. S. Krishnaprasad, Orthogonal Matching Pursuit: recursive function approximation with applications to wavelet decomposition, in *Proceedings of the 27th Asilomar Conference on Signals, Systems, and Computers* (Pacific Grove, CA, USA, 1993) p. 40.
 - [38] Z. Zhang, S. Schwartz, L. Wagner, and W. Miller, A greedy algorithm for aligning DNA sequences, *Journal of Computational Biology* **7**, 203 (2000).
 - [39] R. Ruiz and T. Stützle, A simple and effective iterated greedy algorithm for the permutation flowshop scheduling problem, *European Journal of Operational Research* **177**, 2033 (2007).
 - [40] D. C. van der Laan, J. D. Weiss, and D. M. McRae, Status of CORC cables and wires for use in high-field magnets and power systems a decade after their introduction, *Superconductor Science and Technology* **32**, 033001 (2019).
 - [41] C. Paz-Soldan, Non-planar coil winding angle optimization for compatibility with non-insulated high-temperature superconducting magnets, *Journal of Plasma Physics* **86**, 815860501 (2020).
 - [42] D. W. Dudt and E. Kolemen, DESC: a stellarator equilibrium solver, *Physics of Plasmas* **27**, 102513 (2020).
 - [43] F. Wechsung, M. Landreman, A. Giuliani, A. Cerfon, and G. Stadler, Precise stellarator quasi-symmetry can be achieved with electromagnetic coils, *Proceedings of the National Academy of Sciences* **119**, e2202084119 (2022).
 - [44] D. A. Gates, A. H. Boozer, T. Brown, J. Breslau, D. Curreli, M. Landreman, S. A. Lazerson, J. Lore, H. Mynick, G. H. Neilson, N. Pomphrey, P. Xanthopoulos, and A. Zolfaghari, Recent advances in stellarator optimization, *Nuclear Fusion* **57**, 126064 (2017).
 - [45] Princeton Research Computing, Stellar, <https://researchcomputing.princeton.edu/systems/stellar> (Accessed 2024-01-16).
 - [46] M. Landreman, B. Medasani, F. Wechsung, A. Giuliani, R. Jorge, and C. Zhu, SIMSOPT: a flexible framework for stellarator optimization, *Journal of Open Source Software* **6**, 3525 (2021).
 - [47] P. Ramachandran and G. Varoquaux, Mayavi: 3D visualization of scientific data, *Computing in Science & Engineering* **13**, 40 (2011).
 - [48] H. Frerichs, FLARE: field line analysis and reconstruction for 3D boundary plasma modeling (2024).
 - [49] S. A. Lazerson, J. Schmitt, C. Zhu, J. Breslau, and STELLOPT Developers, STELLOPT, <https://doi.org/10.11578/dc.20180627.6> (2020).
 - [50] Å. Björck, *Numerical Methods for Least Squares Problems*, 2nd ed. (SIAM, 2024).
 - [51] G. H. Golub, J. Lambers, and L.-H. Lim, Lecture notes for CME 302: Numerical Linear Algebra, University of Chicago (2005).
 - [52] M. N. Rosenbluth, R. Z. Sagdeev, J. B. Taylor, and G. M. Zaslavski, Destruction of magnetic surfaces by magnetic field irregularities, *Nuclear Fusion* **6**, 297 (1966).